



Universiteit  
Leiden  
The Netherlands

**X-ray spectroscopy of interstellar dust: from the laboratory to the Galaxy**  
Zeegers, S.T.

**Citation**

Zeegers, S. T. (2018, November 1). *X-ray spectroscopy of interstellar dust: from the laboratory to the Galaxy*. Retrieved from <https://hdl.handle.net/1887/66668>

Version: Not Applicable (or Unknown)

License: [Licence agreement concerning inclusion of doctoral thesis in the Institutional Repository of the University of Leiden](#)

Downloaded from: <https://hdl.handle.net/1887/66668>

**Note:** To cite this publication please use the final published version (if applicable).

Cover Page



Universiteit Leiden



The handle <http://hdl.handle.net/1887/66668> holds various files of this Leiden University dissertation.

**Author:** Zeegers, S.T.

**Title:** X-ray spectroscopy of interstellar dust: from the laboratory to the Galaxy

**Issue Date:** 2018-11-01

# 3

## Dust absorption and scattering in the silicon K-edge

### Abstract

*Context* The composition and properties of interstellar silicate dust are not well understood. In the X-rays, interstellar dust can be studied in detail, by making use of the fine structure features in the Si K-edge. The features in the Si K-edge offer a range of possibilities to study silicon-bearing dust, such as investigating the crystallinity, abundance and the chemical composition along a given line of sight.

*Aims* We present newly acquired laboratory measurements of the silicon K-edge of several silicate-compounds which complement our measurements from our earlier pilot study. The resulting dust absorption profiles serve as templates for the interstellar absorption that we observe. The absorption profiles were used to model the interstellar dust in the dense environments of the Galaxy.

*Methods* The laboratory measurements, taken at the Soleil synchrotron facility in Paris, were adapted for astrophysical data analysis and implemented in the SPEX spectral fitting program. The models were used to fit the spectra of nine low-mass X-ray binaries located in the Galactic center neighborhood in order to determine the dust properties along those lines of sight.

*Results* Almost all lines of sight can be well fitted by amorphous olivine. We also established upper limits on the amount of crystalline material that the modeling allows. We find that iron-poor pyroxenes do not provide a good match to the data. We obtained values of the total silicon abundance, silicon dust abundance and depletion along each of the sightlines. We find a possible gradient of  $0.06 \pm 0.02$  dex/kpc for the total silicon abundance versus the Galactocentric distance. We do not find a relation between the depletion and the extinction along the line of sight.

### 3.1 Introduction

Silicates form an important and abundant component of the interstellar dust (Tielens, 2001). They are found at every evolutionary stage in the life cycle of stars, such as interstellar clouds, the circumstellar environment of oxygen rich Asymptotic Giant Branch (AGB) stars, protostellar disks, meteorites, comets, on Earth and on other planets (Henning, 2010). It is therefore crucial to understand the composition and properties of the silicate dust in order to make correct assumptions about each of the many processes in the universe in which the dust plays a role.

Observations of the gas abundances in interstellar environments have given an indication of the dust composition in the Galaxy. From observations of the Sun, nearby stars and the solar system it is known which elements are expected to be abundant in the ISM. However, certain elements are depleted from the cold gas phase and are assumed to be residing in dust particles (Draine, 2003). Here we define depletion as the ratio of the dust abundance to the total amount of a given element (i.e. both gas and dust). A large fraction of the abundant elements carbon, oxygen, silicon, iron and magnesium are thought to be depleted in dust (Jenkins, 2009; Savage and Sembach, 1996). These elements form the basic constituents of silicates, except for carbon which forms its own grain population of carbonaceous dust (Weingartner and Draine, 2001). However, the precise composition of interstellar silicates remains unknown. The bulk of the interstellar silicate dust is thought to consist of olivine and pyroxene types of dust, with iron and magnesium and smaller contributions of less abundant elements, such as calcium (Tielens, 2001). In addition there may be oxides (e.g. SiO, SiO<sub>2</sub>) present, since they are observed in stellar spectra (Posch et al., 2002; Henning et al., 1995), and silicon could also be present in small amount in the form of silicon carbide (SiC, Kemper et al., 2004; Min et al., 2007).

Much of our knowledge of interstellar silicates comes from the study of infrared absorption and emission features. In the infrared, silicates are mainly observed by using the Si-O bending and stretching modes at 10 and 20  $\mu\text{m}$ . Draine and Lee (1984) used synthetic optical functions in combination with the observational opacities of the 9.7  $\mu\text{m}$  feature to derive an average composition of the silicate dust (called astrosilicate), finding an olivine type with a composition of Mg<sub>1.1</sub>Fe<sub>0.9</sub>SiO<sub>4</sub> and in this way the silicate grains would incorporate 90%, 95%, 94% and 16% of the total Si, Mg, Fe and O, respectively. Nonetheless, interstellar silicates are expected to form a mixture of different silicate types, including olivine, but also, for example, pyroxene. Studies by Kemper et al. (2004), Chiar and Tielens (2006) and Min et al. (2007) compared laboratory spectra with observations and find that a combination of olivine and pyroxene dust models fit the 10  $\mu\text{m}$  feature, although they find varying contributions of olivine and pyroxene as well as for the iron to magnesium ratio.

An important property of the dust is the crystallinity, from which we can learn about the formation history of the dust. However, the formation process of crystalline dust is not well understood (Speck et al., 2011). We know, from observations of circumstellar dust, that evolved oxygen rich AGB stars produce silicate dust and that up to about 15% of this dust is in crystalline form. The dust is then subsequently injected in the ISM by stellar winds (Sylvester et al., 1999; Kemper et al., 2004). Crystalline dust is thought to be formed close to the star and is expected to be mostly magnesium rich. Further from the star the temperatures are lower and the silicates do not get the opportunity to crystallize (Molster et al., 2002). However,

this formation process of crystalline dust is not certain. Speck et al. (2015) found crystalline dust at the outer edge of the star HD 161796 and amorphous dust in the inner part of the dust shell. They propose that crystallization may happen when the dust encounters the ISM. Further away from dust forming stars, in the diffuse ISM, the smooth features of the  $\sim 10\ \mu\text{m}$  and  $\sim 20\ \mu\text{m}$  indicate that most of the interstellar dust appears amorphous. Only 1.1% of the dust along the lines of sight toward carbon-rich Wolf-Rayet stars near the center of the Galaxy appears to be crystalline (Kemper et al., 2004). From the mass budget of stellar dust sources the amount of crystalline dust in the ISM is expected from the to be  $\sim 5\%$  (Kemper et al., 2004), which suggests considerable re-processing of the dust in the ISM. Over time, the silicates may lose their crystalline structure in the violent environment of the ISM, where the dust is bombarded by radiation and cosmic rays on a timescale of  $\sim 70\ \text{Myr}$  (Bringa et al., 2007). These processes may be the cause of the amorphisation of crystalline dust in the ISM (Jäger et al., 2003, and references therein). Interestingly, silicates are again abundant in crystalline form in proto-planetary disks. The cores of some interstellar grains retrieved by the stardust mission, also show the presence of crystalline dust (Westphal et al., 2014), showing the possibility that at least some of the crystalline interstellar dust may survive in the ISM.

The soft X-ray part of the spectrum provides an alternative wavelength range for the study of interstellar dust (Draine, 2003; Lee et al., 2009; Costantini et al., 2012). X-ray binaries are used as a background source to observe the intervening gas and dust along the line of sight. In the spectra of these X-ray binaries, we can observe several absorption edges. Depending on the column density along the line of sight and the brightness of the source, it is possible to access the absorption edges of different elements. X-ray Absorption Fine Structures (XAFS) near the atomic absorption edges of elements can be used as a unique fingerprint of the dust along the line of sight toward the source. XAFS are observed in X-ray spectra of various astrophysical sources of *Chandra* and *XMM-Newton* (Lee et al., 2001; Ueda et al., 2005; Kaastra et al., 2009; de Vries and Costantini, 2009; Pinto et al., 2010, 2013; Costantini et al., 2012; Valencic and Smith, 2013; Zeegers et al., 2017, Chapter 2). These provide a powerful tool to study the composition, abundance, crystallinity, stoichiometry, and size of interstellar silicates (de Vries and Costantini, 2009, Chapter 2).

Interstellar dust may show slight variations in different environments. For example, from dense molecular clouds we know, that dust may incorporate a layer of ice around the grains, but also in less dense environments the dust may show variations in composition and properties. For instance, the abundances of several elements, show a decrease with distance from the Galactic center (Rolleston et al., 2000; Chen et al., 2003; Davies et al., 2009). The ISM is also known to be patchy and therefore may allow the observation of local differences in the chemistry along different lines of sight (Bohlin et al., 1978; Nittler, 2005). The X-rays provide the possibility to study dust in different environments. In this study, we focus on the silicon K-edge, which gives access to denser regions in the central part of the Galaxy.

In our pilot study, we showed the analysis of the silicon K-edge of GX 5-1 (Chapter 2). Here we expanded the number of sources we study to a total of nine. Furthermore, we expanded the set of silicate samples with respect to the previous study from six to fifteen. The sample set contains the interstellar dust analogues pyroxenes, olivines and silicon dioxide, that can be used to analyze interstellar silicate dust. These measurements are part of a larger laboratory measurement campaign (Costantini and de Vries, 2013).

The chapter is structured in the following way: In Section 3.2 we explain the analysis of

our laboratory data and the use of XAFS to investigate the composition of interstellar dust. In Section 3.3 we explain how we obtained the extinction cross-section and implemented them in the extinction profiles that can be used as interstellar dust models in an X-ray fitting code. In Section 3.4 we show the source selection, data and spectral analysis. In Section 3.5 we discuss the results and the chemistry of the dust toward the dense central area of the Galaxy. Lastly, in Section 3.6, we give a summary and our conclusion.

## 3.2 X-ray absorption edges

### 3.2.1 The samples

In this analysis, we make use of 14 different dust samples for which we measured the Si K-edges. The composition and structure of these dust samples are listed in Table 3.1, where the first five samples are the same as in Chapter 2. The additional samples, 6 to 14, were measured in January 2017 at the Soleil synchrotron facility in Paris.

There are several olivine- and pyroxene-type silicates among the samples, as well as different types of quartz. Although technically quartz types (samples 13-15) are oxides, we will refer to all the samples in the paper as silicates. Samples 2, 3, 5, 6, 7, 8, and 10 were synthesized for this analysis in laboratories at AIU Jena and Osaka University. In particular, the amorphous samples (2, 5, 7, 8 and 10) have been synthesized by quenching of a melt according to the procedure described by Dorschner et al. (1995). There are also synthesized crystalline samples in the sample set, such as fayalite (sample 9). The crystals of this sample have been grown by a method called the ‘scull method’ (Lingenberg, 1986). More details about samples 1-5 can be found in Zeegers et al. 2017 and more details about samples 6-15 can be found in Table 3.1.

The samples were all chosen because of their relevance as a possible component of the silicate dust in the ISM. We used the following criteria in the selection of this sample set:

- The sample set consists out of pyroxenes, olivines and oxides
- The silicate samples have different iron to magnesium ratios
- The samples contain both amorphous and crystalline silicates

The motivation of these selection criteria is based primarily on Draine and Lee (1984), who derived a general composition of ‘astronomical silicate’ based upon infrared emissivities inferred from observations of circumstellar and interstellar grains. The composition of this silicate is used as a starting point for the composition of the silicates in our sample set. The content of the sample set is then more refined by involving the results of detailed studies of the 9.7 and 18  $\mu\text{m}$  features in the infrared, which give an indication of the silicate dust composition. Since we expect amorphous silicates to be abundantly present (Kemper et al., 2004), the sample set contains seven amorphous samples of which six have a different composition, one olivine, two quartz types and four pyroxenes. From studies in the 8 – 13  $\mu\text{m}$  band it can be concluded that a mix of predominantly pyroxenes and olivines fit the observed spectra well (Kemper et al., 2004; Chiar and Tielens, 2006; Min et al., 2007). While Kemper et al. (2004) find that olivine dust dominates by mass in the ISM, Chiar and Tielens (2006) find that pyroxene dominates. Both pyroxenes and olivines are therefore well represented in

Table 3.1: Samples

No.	Name	Chemical formula	Structure
1	Olivine	$\text{Mg}_{1.56}\text{Fe}_{0.4}\text{Si}_{0.91}\text{O}_4$	crystal
2	Pyroxene	$\text{Mg}_{0.9}\text{Fe}_{0.1}\text{SiO}_3$	amorphous
3	Pyroxene	$\text{Mg}_{0.9}\text{Fe}_{0.1}\text{SiO}_3$	crystal
4	Enstatite	$\text{MgSiO}_3$	crystal*
5	Pyroxene	$\text{Mg}_{0.6}\text{Fe}_{0.4}\text{SiO}_3$	amorphous
6	Pyroxene	$\text{Mg}_{0.6}\text{Fe}_{0.4}\text{SiO}_3$	crystal
7	Olivine	$(\text{Mg}_{0.5}\text{Fe}_{0.5})_2\text{SiO}_4$	amorphous
8	Pyroxene	$\text{Mg}_{0.75}\text{Fe}_{0.25}\text{SiO}_3$	amorphous
9	Fayalite	$\text{Fe}_2\text{SiO}_4$	crystal
10	Enstatite	$\text{MgSiO}_3$	amorphous
11	Forsterite	$\text{Mg}_2\text{SiO}_4$	crystal
12	Quartz	$\text{SiO}_2$	crystal
13	Quartz	$\text{SiO}_2$	amorphous
14	Quartz	$\text{SiO}_2$	amorphous

\*Sample 4 contains a very small amount iron, which is not significant in our analysis. The Fe:Mg ratio is  $4 \times 10^{-2}$ . Sample 6 is a pyroxene and the crystalline counterpart of sample 5. Sample 7 is an amorphous olivine with equal contributions of iron and magnesium. Sample 8 is an amorphous pyroxene with an iron to magnesium ratio of 1:3. Sample 9, fayalite, was synthesized at the at the University of Frankfurt, Physical Institute (Fabian et al., 2001). Sample 10 is an amorphous enstatite, which was synthesized at AIU Jena. Sample 11, forsterite, is a commercial product from the company Alfa Aesar. Sample 12 is a natural rock crystal from Brazil (Zeidler et al., 2013). Sample 13, an amorphous silica, is a commercial product of company Qsil Ilmenau, Germany, named “ilmasil”. Sample 14, is a commercial amorphous silica powder supplied by the company Fisher Scientific. Sample 13 and 14 differ in degree of amorphisation as can be observed by the XAFS in the lower right panel of Figure 3.16 in Appendix 3.B.

our sample set. Furthermore, different values of the Mg/Fe ratio have been found in silicate dust in the ISM (Kemper et al., 2004; Min et al., 2007). In order to be able to investigate this ratio, we use dust samples with different iron to magnesium ratios. In the case of olivine type silicates we explore both extremes, namely fayalite and forsterite. Fayalite is the iron end-member of the olivine-group, whereas forsterite is the magnesium end-member. Our sample also contains an amorphous olivine with equal amounts of iron and magnesium.

### 3.2.2 Analysis of laboratory data

A self-evident method to measure the degree of absorption of a sample would be to measure the transmission of the radiation through the sample. This can be done by measuring the ratio of the intensity of the incoming beam to that of the transmitted beam. In order to appear optically thin at the energy around the Si K-edge, such a measurement would require a sample thickness of  $1.0 - 0.5 \mu\text{m}$ . It is impractical to perform measurements with such thin samples at X-ray energies. Therefore, the degree of absorption of the samples cannot be measured directly through transmission. Instead, the absorption is derived from the fluorescent measurements of the Si  $K\alpha$  line in our analysis of the Si K-edge. An overview of the theory behind this method can be found in Section 2.3.2 of Chapter 2.

The fluorescent measurements of the samples were performed at the SOLEIL synchrotron facility in Paris using the LUCIA beamline (Flank et al., 2006). The first run was completed and published in Chapter 2, the second run was completed in 2017 and presented in this chapter. All the samples were pulverised into a fine powder. This powder was then pressed into a layer of indium, which was stuck on a copper sample plate. The sample plate was placed in the X-ray beam in a vacuum environment. The reflecting fluorescent signal was measured by a silicon drift diode detector. Each sample was measured at two different positions on the sample plate and for each position the measurement was repeated once, resulting in a total of four measurements per sample. The change in position is necessary to avoid any dependence of the measurement on the position of the sample on the copper plate. We took the average of the resulting four measurements. In order to obtain the noise in the measurements, we determined the dispersion among the measurements. We found a small dispersion of 5% among the measurements. This is slightly higher than in our previous sample set of Chapter 2, but still considered negligible. After the measurements have been obtained they need to be corrected for two effects, namely pile-up and for saturation. Pile-up occurs when two photons hit the detector at once and are recorded as one event with double the energy. This effect can be seen in the spectrum as a spurious line appearing at twice the expected energy. This effect is, however, minimal ( $< 1\%$ ). Saturation occurs because the measured fluorescent signal is not directly proportional to the absorption. The effect of saturation becomes important when a sample is concentrated, which is the case here (de Groot, 2012). We use the program FLUO to correct for saturation when needed (Stern et al., 1995). More details can be found in Chapter 2, since here we follow the same correction procedure. We note that a crystalline pyroxene was omitted from our sample set, which is present in Chapter 2 and indicated there as sample 6. The correction is on average three times larger than in the other samples, which indicates that the sample could be overcorrected after the application of FLUO. The overcorrection may be the result of a mismatch between the given composition and the measured compound, although this may not necessarily be the case (Ravel and Newville, 2005). However, since the cause of the large correction could not be retrieved in this case, the sample was removed from sample set.

### 3.2.3 X-ray Absorption Fine Structures

XAFS are modulations that arise when an X-ray photon excites a core electron in an atom. These modulations are a fingerprint of the type of dust and can therefore be used to discriminate between different types of dust in the ISM. XAFS arise from the wave-like nature of the photoelectric state. When a core electron is excited by an incoming X-ray with the right energy, the ionized electron will then behave like a photoelectron. This can be interpreted as a wave emanating from the site of the absorbing atom. Depending on the available energy, the photoelectron can scatter around the neighboring atoms. Due to this interaction, the initial wave is scattered and new waves emanate from the neighboring atoms. These waves are superimposed on the original wave creating interference. This subsequently changes the probability of the photoelectric effect. We observe the constructive and destructive interference in the edge as a function of energy, i.e. the XAFS. Depending on the elements and the position of the neighboring atoms, the XAFS are modified in a unique way, reflecting the crystallinity and chemical composition of the material.

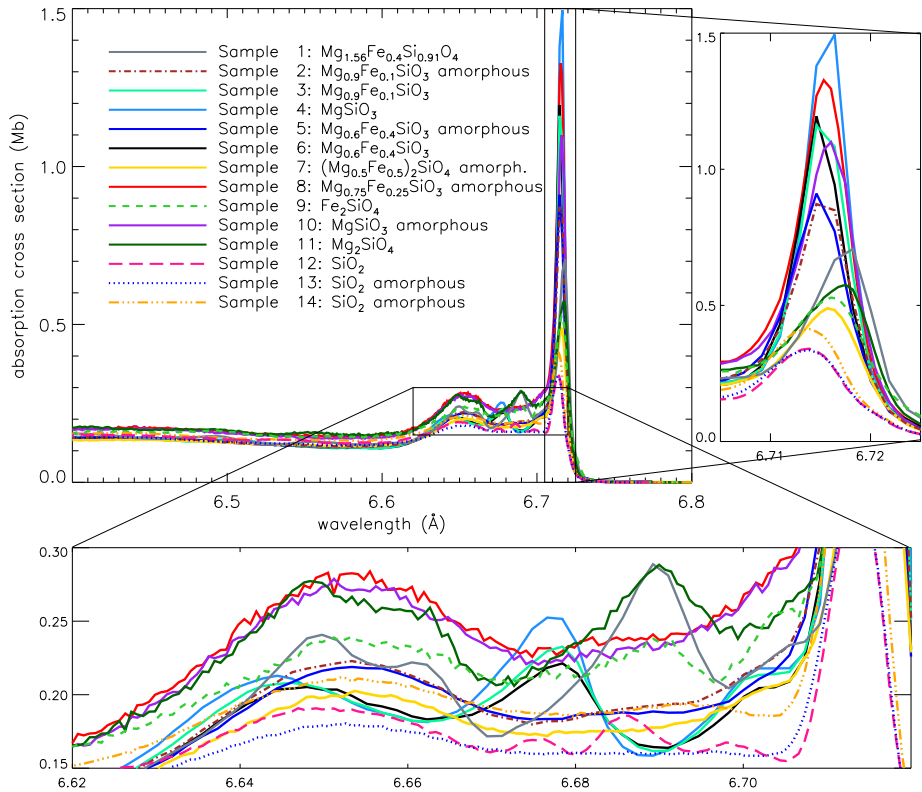


**Figure 3.1:** The Si K-edge of dust samples 1-14 (samples 1-5 are also shown in Chapter 2). The x-axis shows the energy in Å and the y-axis shows the amount of absorption indicated by the cross-section (in Mb per Si atom).

The resulting absorption cross-sections can be found in Figure 3.1. We highlight the XAFS in the left inset panel. Samples 2, 5, 7, 8, 10, 13 and 14 are amorphous. Since these amorphous samples do not have a regular crystalline structure, they lose the distinct signature which is present in their crystalline counterparts. This effect can be observed in Figure 3.1 between 6.67 and 6.70 Å. The XAFS of amorphous materials are very similar in shape, as can be observed by comparing sample 7, 8 and 10. It is therefore difficult to distinguish an amorphous pyroxene and an amorphous olivine. The differences between these edges will then also depend on slight shifts in the ionisation energy and the peak intensity at this energy. This is shown by the inset panel on the right of Figure 3.1. In the case of sample 12, 13 and 14 we can compare three samples of which the composition is the same, but the crystallinity varies. It can be observed that the resulting absorption cross-sections of quartz are very similar since the composition does not change between the samples, but that the crystalline sample shows features between 6.67 and 6.70 Å. Distinct differences can be observed in the case of the crystalline pyroxene of sample 7 and forsterite (sample 12) around 6.66 and 6.70 Å, illustrating the difference between crystalline pyroxene-type silicates and crystalline olivine-type silicates. The effect of the varying iron content of the samples is subtler and shows itself by shifts in the peak of the XAFS (e.g. samples 9 and 11). Furthermore, the samples can also be characterized by the peak strength of the edge between 6.71 and 6.72 Å and the energy position of this peak.

### 3.3 Extinction cross sections

The extinction cross-sections for each of the samples can be derived from the laboratory data. In this section, we will give a summary of the methods that are used to derive the cross-sections. For a full description about the calculation of the extinction cross-section we refer to Chapter 2. From the laboratory data, we obtain the attenuation coefficient ( $\alpha$ ). The Beer-Lambert law can be used to derive  $\alpha$ :

$$T = \frac{I}{I_0} = e^{-\alpha x} = e^{-x/l}. \quad (3.1)$$

Here  $T$  is the transmittance, which can be obtained by assuming an optically thin sample thickness  $x$  and by using tabulated values of the mean free path  $l$  (e.g., the average distance travelled by a photon before it is absorbed), provided by the Center for X-ray Optics (CXRO) at Lawrence Berkeley National laboratory. The laboratory absorption edges were transformed into transmission spectra and fitted to the transmittance  $T$  obtained from tabulated transmission data, as well provided by CXRO. Consequently, from  $\alpha$  the imaginary part of the refractive index  $k$  can be derived, since the attenuation coefficient can be described as:

$$\alpha = \frac{4\pi k}{\lambda}, \quad (3.2)$$

where  $\lambda$  is the wavelength. The real part of the refractive index is then calculated by using a numerical solution to the Kramers-Kronig relations (Bohren, 2010). The method used for this calculation is the same as in Chapter 2, namely the fast Fourier transform routines (FFT) as described in Bruzzoni et al. (2002). We use Mie theory (Mie, 1908) to calculate the extinction efficiency at each wavelength and grain size. The grain size distribution used in this analysis is

the MRN distribution, with a grain size range of  $0.005 - 0.25 \mu\text{m}$ . The grains are modelled as solid spheres. The MIEVO code (Wiscombe, 1980) was used to calculate the extinction efficiency, which needs the optical constants, wavelength and grain size as input parameters. From the obtained extinction efficiency we calculate the extinction cross-sections. These extinction cross-section are implemented in the AMOL model of the fitting code SPEX (Kaastra et al., 1996), where they are used for further analysis. Figure 3.15 shows the resulting extinction profiles of each of the dust models. The absolute cross-section are available in tabular form<sup>1</sup>.

## 3.4 Data analysis of the LMXB

### 3.4.1 Source selection

We selected nine low mass X-ray binary sources for our analysis from the *Chandra* Transmission Gratings Catalog and Archive<sup>2</sup>. The selection depends on the brightness of the source and the hydrogen column density  $N_{\text{H}}$  towards the source. In order to have the best view of the silicon K-edge, the column density of the source should be between  $10^{22}$  and  $10^{23} \text{cm}^{-2}$ . It is furthermore important that the source is bright in order to observe the edge with a high signal to noise. The flux level needs to be  $> 0.5 \times 10^{-12} \text{erg cm}^{-2}\text{s}^{-1}$  at energies between 0.5–2 keV. The source should preferably not strongly fluctuate in brightness, since this will affect the quality of the edge in the spectrum. We therefore inspected the light curves for strong dips in the brightness. We did not find this to be a problem in any of the selected sources. Sources with the desired column density lie preferentially around the Galactic Center (GC) area (Table 3.2).

Another more practical selection criterion is that the source has to be observed in TE mode. The ACIS detectors on-board *Chandra* can operate in different observing modes, namely continues clocking (CC) mode and timed exposure (TE) mode. The CC mode is not suitable for measurements of the Si K-edge since the edge is filled by the bright scattering halo radiation of the source. The edge has a different optical depth in comparison with the TE mode and seems slightly smeared. The effect of the scattering halo is particularly evident in the CC mode because the two arms of the mode are now compressed into one. An overview of the sources that are used in this study is given in Table 3.2. Here we also indicate the OBSIDs of the spectra of the sources, the distance and the Galactic coordinates.

### 3.4.2 Modeling procedure

After the selection of the sources as described in the previous section, we inspected the spectra for pile-up. Pile-up occurs when two or more photons are detected as one single event and therefore occurs often in the spectra of bright sources, such as the X-ray binaries used in this work. Both gratings (HEG and MEG) are affected, but the effect is especially evident in the MEG grating. The parts of the spectra of the MEG grating that were too affected by pile-up were ignored. This was done in the case of all the X-ray binaries, but the ignored range varies per source. This is described for each individual source in Appendix 3.A. Before we can

<sup>1</sup> [www.sron.nl/~elisa/VIDI/](http://www.sron.nl/~elisa/VIDI/)

<sup>2</sup> <http://tgcatalog.mit.edu/>

Table 3.2: Sources

Name	obsid(s)	distance	coordinates	
		kpc	$l$ (deg)	$b$ (deg)
GX 5-1	19449, 20119	$9.2^1$	5.08	-1.02
GX 13+1	11814, 11815, 11816, 11817	$7 \pm 1^2$	13.52	+0.11
GX 340+00	1921, 18085, 19450, 20099	$11 \pm 0.3^3$	339.59	-0.08
GX 17+2	11088	$12.6^4$	16.43	+1.28
4U 1705-44	5500, 18086, 19451, 20082	$7.6 \pm 0.3^5$	343.32	-2.34
4U 1630-47	13714, 13715, 13716, 13717	$10^6$	336.91	+0.25
4U 1728-34	2748	$5.2 \pm 0.5^7$	354.30	-0.15
4U 1702-429	11045	$7^8$	343.89	-1.32
GRS 1758-258	2429, 2750	$8.5^9$	4.51	-1.36

All observations were done in TE mode. Christian and Swank (1997)<sup>1</sup> Bandyopadhyay et al. (1999)<sup>2</sup> Christian and Swank (1997)<sup>3</sup> Lin et al. (2012)<sup>4</sup> Galloway et al. (2008)<sup>5</sup> Parmar et al. (1986); Augusteijn et al. (2001)<sup>6</sup> Galloway et al. (2008)<sup>7</sup> Oosterbroek et al. (1991)<sup>8</sup> Keck et al. (2001)<sup>9</sup>

study the interstellar dust, we first have to model the underlying continuum of each source and inspect the spectra for the presence of outflowing ionized gas and hot gas present along the line of sight, as described in Sections 3.4.2.1 and 3.4.2.2.

### 3.4.2.1 Continuum and neutral absorption

The underlying continuum of each source is fitted using the spectral analysis code SPEX. We tested several additive SPEX models in our analysis, namely blackbody, disk-blackbody, power law and Comptonisation models. The X-ray radiation from the source is then absorbed by a neutral absorber. This model is represented by the multiplicative HOT model in SPEX. In order to mimic a neutral cold gas, the temperature of this gas is frozen to a value of  $kT = 5 \times 10^{-4}$  keV. After obtaining a best fit for the continuum with absorption of neutral cold gas we are able to determine the column density of hydrogen toward the source.

We will use GX 5-1 as an example to explain our method of fitting the sources. The results of the best fits of the other X-rays binaries and the details of the fitting method used in each case can be found in Appendix 3.A. Two spectra were used in the fit of GX 5-1, with obsids 19449 and 20119. These observations have an excellent signal-to-noise ratio, in the case of obsid 19449 this is around the Si K-edge  $S/N \approx 100$  per bin and for obsid 20119  $S/N \approx 60$  per bin. The MEG grating shows signs of pile up in both data sets above an energy of 2.5 keV and the data was therefore ignored above this value of the energy. Since the Silicon K-edge starts around 1.84 keV the MEG data is included in the analysis of the edge. This is the case for every X-ray binary in our analysis. We used a Comptonisation model and a disk-blackbody model to describe the underlying continuum of GX 5-1. We found a column density of  $5.8 \pm 0.2 \times 10^{22} \text{cm}^{-2}$ . The broadband fit of GX 5-1 is shown in Figure 3.2. For clarity, the data displayed in this figure belongs to obsid 19449, since this dataset dominates the fitting of the spectrum due to its superior quality. The fit already includes the dust model of which the details are described in Section 3.4.2.3. The parameter values of the best fit of

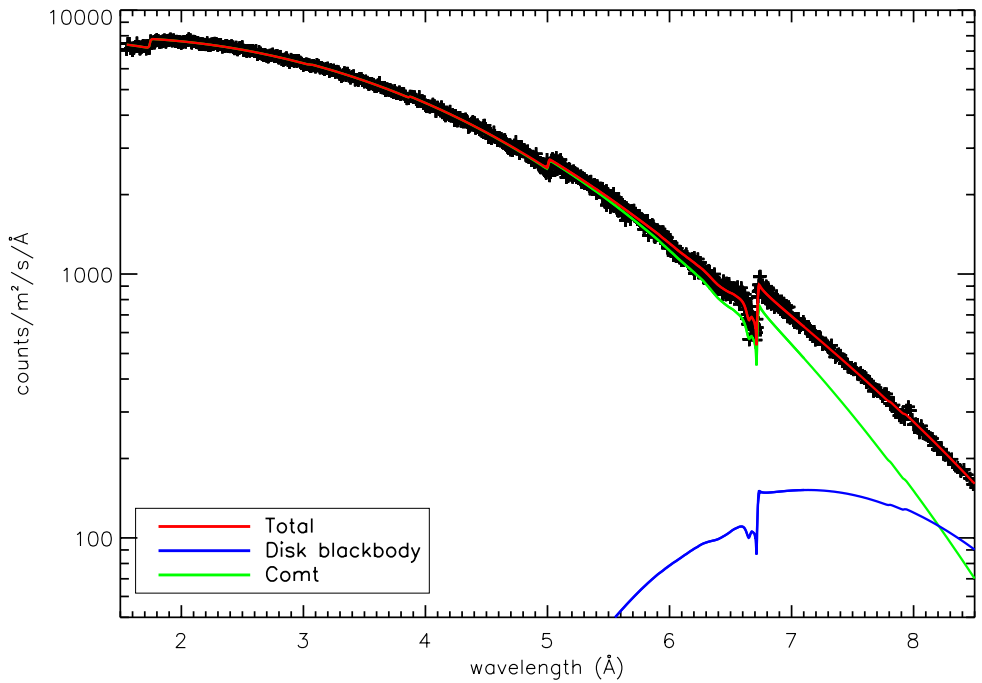


Figure 3.2: Broad band fit of GX 5-1 with the data of obsid 19449 with the disk blackbody model indicated by the blue line and the green line indicates the Comptonisation model. The red line shows the total fit. The AMOL dust models are included in the fit.

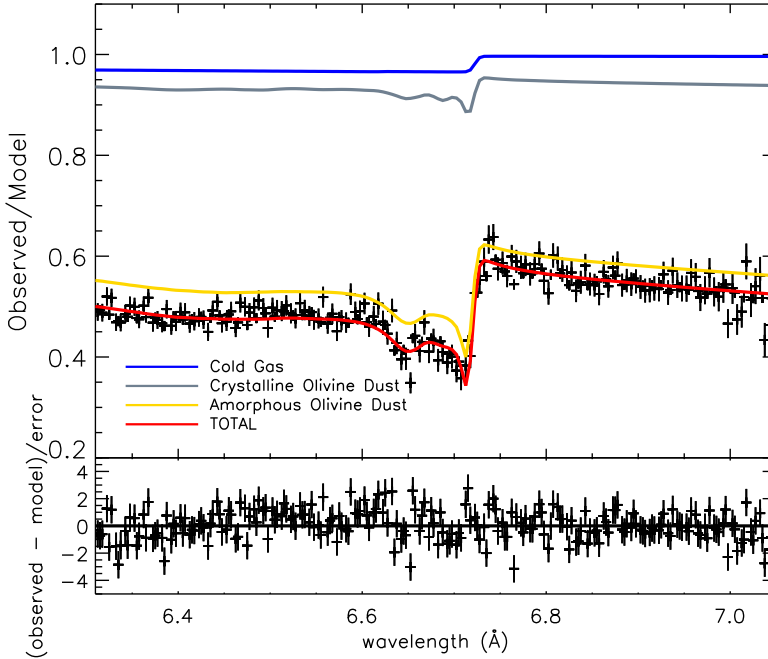


Figure 3.3: Fit of the Si K-edge of X-ray binary GX 5-1. The best fitting dust mixture is shown by the yellow line (amorphous olivine, sample 8) and the grey line (crystalline olivine dust, sample 1). The cold gas contribution is shown by the blue line and the total, cold gas and dust, by the red line.

GX 5-1 can be found in Table 3.5. Errors given on parameters are 1 sigma errors, which is the case for all errors shown in this analysis.

#### 3.4.2.2 Hot ionized gas on the line of sight in the Si K-edge region?

We tested whether there was hot gas along the line of sight towards the sources (fitted in the spectra using again the HOT model, which has a tuneable temperature), as well as outflowing ionized gas related to the source (fitted in the spectra using the XABS model of SPEX). If absorption lines of this gas appear near the edge, it is important to take these lines into account for accurate modeling.

We found outflowing gas from the source in two cases, namely for GX 13+1 and 4U 1630-47. These sources show strong absorption lines in their spectra. In the case of GX 13+1, a second, but non-outflowing, ionized gas component was also found (Table 3.7).

Collisionally ionized hot absorbing gas in the ISM is thought to have temperatures between  $\sim 10^6 - 10^7$  K (Yao and Wang, 2007; Wang, 2009; Wang et al., 2013). For GRS 1758-258, GX 17+2 and 4U 1705-44 a hot component was found with temperatures within

the range mentioned, namely  $1.5^{+0.6}_{-0.3} \times 10^7$  K,  $1.6 \pm 0.2 \times 10^6$  K and  $2.1^{+0.9}_{-0.6} \times 10^6$  K, respectively. The hydrogen column density of the gas is for all sources of the order of  $10^{20}$  cm<sup>-2</sup>, (Table 3.9), which is in correspondence with the typical expected hydrogen column densities of such a gas (Yao and Wang, 2005; Yao et al., 2006; Yao and Wang, 2007). We did not find evidence for outflowing ionized gas along the line of sight of GX 5-1 and neither did we find any contribution of hot gas. This is also the case for 4U 1702-429, 4U 1728-34 and GX 340+00. The values of the parameters of the HOT and the XABS model can be found in the tables with the best fits of the sources in Appendix 3.A.

### 3.4.2.3 Dust Mixtures and the SPEX AMOL model

After obtaining the underlying continuum and the column density of hydrogen towards the source, we proceed by adding the dust model to the fit. We also take into account the presence of hot and outflowing ionized gas along the line of sight as mentioned in Section 3.4.3. The AMOL routine in SPEX is used to fit the dust models to the data. AMOL can fit four dust models simultaneously. We want to test all possible unique combinations of the 14 dust models. To execute these fits, we follow the method of Costantini et al. (2012), namely the total number of fits ( $n$ ) is given by  $n = n_{\text{dust}}! / (4!(n_{\text{dust}} - 4)!)$  and where  $n_{\text{dust}}$  is the number of available dust models and 4 is the number of models that can be tested in the same run. This results in 1001 possible unique combinations to fit the 14 dust models.

From all these combinations, we can select the best fitting mixture. Of each possible dust mixture, we determined the reduced  $C^2$  values. All the fits in this chapter generated by SPEX are using C-statistics (Cash, 1979) as an alternative to  $\chi^2$ -statistics. C-statistics may be used regardless of the number of counts per bin, therefore we can use bins with a low count rate in the spectral fitting. The best fit is given by the lowest reduced  $C^2$  value (Kaastra, 2017). As an example, we show the resulting best fit of GX 5-1 in Figure 3.3. Here we show the contribution of cold gas, and the two best fitting dust samples in the mixture: sample 1 crystalline olivine contributing 11% and sample 7 amorphous olivine contributing 89% to the total column density of silicon in dust. The other two samples in the mix do not contribute significantly. The best fits of the sources in our sample are described in Section 3.5.

In Figure 3.4 the best fitting dust mixtures of all nine X-ray binaries considered here are indicated by the green bars. On the x-axis we show the numbers belonging to each dust sample, which can be retrieved from Table 3.1. The y-axis indicates the relative contribution of each of the dust sample in the fit with respect to the dust column density of silicon. The best fits represent one of the 1001 possible dust mixtures per source and it is useful to take the performance of the other dust mixtures into account before discussing the results. Therefore, an insightful way to study whether a certain dust mixture fits the edge well, is by showing how much a dust mixture deviates from the best fitting mixture. Each dust mixture is represented in Figure 3.4 by four colored filled circles, i.e. the number of dust samples per fit. The position of the filled circles on the y axis shows the contribution of the dust sample to the fit. For each of the 1001 dust mixtures a set of four filled circles is plotted. The colors of the filled circles correspond with the one, two and three sigma deviations from the best fit, as shown in the legend of Figure 3.4.

In the ideal case, the dust samples that correspond with the best fit, will also be represented in the results of similar dust mixtures. In the case of GX 5-1 for instance, the best fit consists

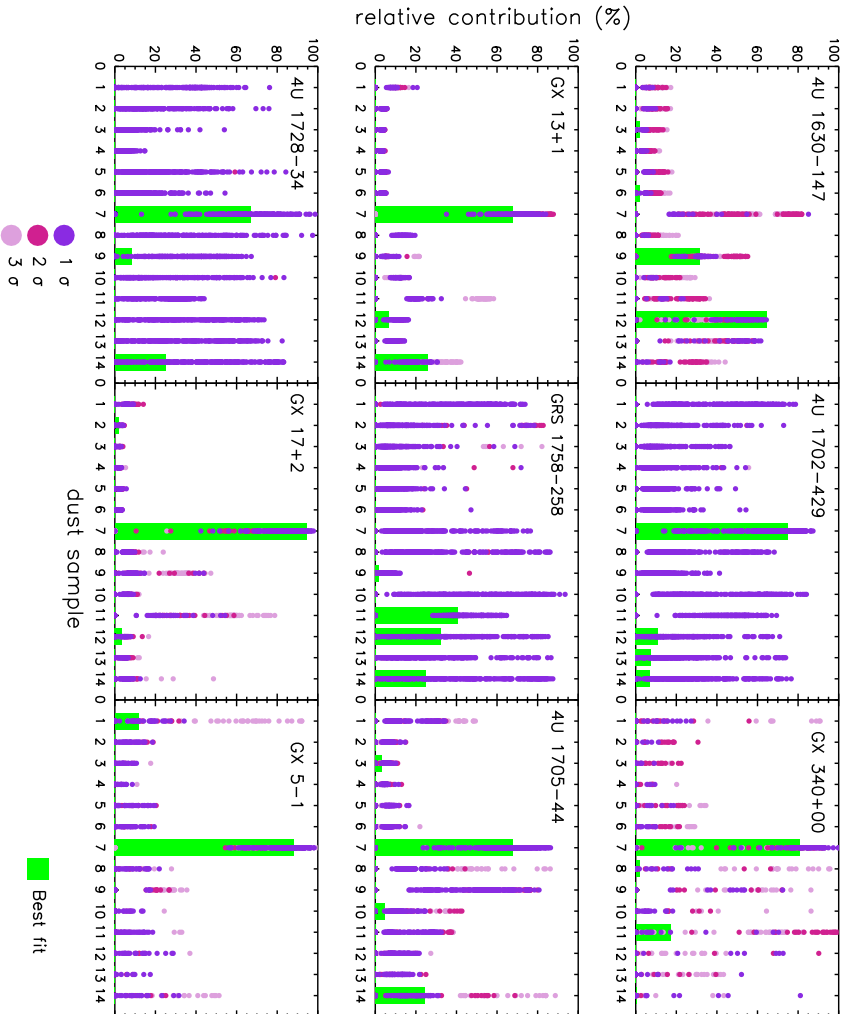


Figure 3.4: The figure shows best fitting dust mixtures in comparison with other possible dust mixtures. In green the relative contribution of each of the dust components in the best fit is shown. The other dust mixtures are represented by the colored dots. The colors indicate the 1, 2 and 3 sigma deviations from the best fitting dust mixture. Per fit 4 dust samples are fitted to the spectra of the X-ray binaries.

Table 3.3: Abundances and depletions of Silicon

Source	$N_{\text{Si}}^{\text{tot}}$ ( $10^{18} \text{ cm}^{-2}$ )	depletion	$A_{\text{Si}}$ ( $10^{-5} \text{ H atom}^{-1}$ )	$A_{\text{Si}}^{\text{dust}}$ ( $10^{-5} \text{ H atom}^{-1}$ )	$A_{\text{Si}}/A_{\odot}$
GX 5-1	$1.7 \pm 0.2$	$0.89 \pm 0.05$	$2.9 \pm 0.2$	$2.5 \pm 0.2$	$0.8^{+0.2}_{-0.1}$
GX 13+1	$1.4 \pm 0.2$	$0.94 \pm 0.02$	$4.6 \pm 0.7$	$4.4 \pm 0.7$	$1.2 \pm 0.2$
GX 340+00	$2.9 \pm 0.6$	$0.77 \pm 0.10$	$4.5 \pm 0.9$	$3.6 \pm 0.9$	$1.2^{+0.2}_{-0.3}$
GX 17+2	$1.1 \pm 0.2$	$0.95 \pm 0.03$	$5.2 \pm 0.4$	$5.1 \pm 0.4$	$1.3 \pm 0.1$
4U 1705-44	$0.9 \pm 0.2$	$0.91 \pm 0.05$	$4.3 \pm 1.1$	$4.0 \pm 1.1$	$1.1 \pm 0.3$
4U 1630-47	$4.8 \pm 1.3$	$0.76^{+0.23}_{-0.28}$	$4.9 \pm 1.3$	$4.5 \pm 1.3$	$1.3 \pm 0.4$
4U 1728-34	$1.4 \pm 0.4$	$0.95^{+0.02}_{-0.10}$	$4.1 \pm 1.4$	$3.9 \pm 1.4$	$1.1 \pm 0.4$
4U 1702-429	$0.7 \pm 0.3$	$0.93 \pm 0.15$	$3.2 \pm 1.5$	$3.0 \pm 1.5$	$0.8 \pm 0.4$
GRS 1758-258	$1.0 \pm 0.4$	$0.75 \pm 0.2$	$3.9 \pm 1.5$	$2.9 \pm 1.5$	$1.0 \pm 0.4$
average	$1.8 \pm 0.2$	$0.87 \pm 0.04$	$4.0 \pm 0.4$	$3.8 \pm 0.4$	$1.1 \pm 0.1$

Abundances are indicated by  $A_{\text{Si}}$ . Solar abundances are taken from Lodders and Palme (2009).  $N_{\text{Si}}^{\text{tot}}$  indicates the total column density of silicon (gas and dust).

of two dust samples, leaving two options open, which in the case of the best fit does not contribute significantly. This means that out of the 1001 possibilities, there are 91 similar mixtures as can be seen in Figure 3.4 by the dominant selection of samples 1 and 7. In the case that the best fit is unique we expect a clustering of the similar mixtures around the best fit. This effect can be observed in the frame of GX 13+1 in Figure 3.4 for sample 7 and in lesser degree in GX 5-1 for sample 1 and 7.

If the data are of good quality (i.e. high signal to noise), which is the case for six out of the nine X-ray binaries, it becomes possible to observe a preference in the fits for certain dust samples. This is especially evident in GX 5-1, GX 17+2 and GX 13+1. When the quality of the data declines, it allows almost every type of dust to be fitted equally well. This effect can be observed in the observations of 4U 1702-49, GRS 1758-258 and 4U 1728-34. Therefore, we will not use these sources in the discussion of the dust composition. The implications of Figure 3.4 will be discussed in Section 3.5.1.

### 3.4.3 Silicon abundances and depletion

The silicon K-edge allows the possibility of evaluating silicon in both gas and dust simultaneously. Consequently, this allows a study of the abundance and depletion of silicon on the nine different lines of sight towards the X-ray binaries. Table 3.3 gives the silicon column density ( $N^{\text{tot}}$ ), depletion, total silicon abundance ( $A_{\text{Si}}$ ), abundance of silicon in dust ( $A_{\text{Si}}^{\text{dust}}$ ). Finally,  $A_{\text{Si}}/A_{\odot}$  shows the deviation from the solar abundance of silicon. The allowed depletion ranges used in the fits are based upon values from Jenkins (2009). The ranges of are given in Table 3.4. Since we fit only one edge using dust models, we need to constrain the other elements within reasonable boundaries. For the edges, for which we do not have dust features, we use gas absorption-like profiles in the SPEX model.

Table 3.4: Depletion ranges used in the spectral fitting

Element	depletion range
Silicon	0.41 – 0.96
Iron	0.7 – 0.97
Magnesium	0.47 – 0.95
Oxygen	0.02 – 0.42

Depletion ranges in this table are based on depletion values from Jenkins (2009).

## 3.5 Discussion

### 3.5.1 Dust composition toward the Galactic Center

The results of the fits of the nine X-ray binaries are summarized in Figure 3.4. Since this figure contains information about the crystallinity, the mineralogy, and the ratio between iron and magnesium, we discuss each of the properties of the dust separately. We will also put emphasis on the results of the fits of GX 5-1, GX 13+1 and GX 17+2, since for these sources the quality of the data in terms of signal-to-noise around the Si K-edge is the best with respect to the other sources.

#### 3.5.1.1 Crystallinity

From the fits of all the X-ray binaries we observe that crystalline dust models can be fitted to the Si K-edge. We calculate the ratio of crystalline versus amorphous dust ( $\zeta_1$ ). The ratio here is defined as:  $\zeta_1 = \text{crystalline dust} / (\text{crystalline dust} + \text{amorphous dust})$ . Examining the best fitting dust mixture of GX 5-1, we find a value of:  $\zeta_1 = 0.12$  and when considering the errors we find an upper limit of on the crystallinity of  $\zeta_1 < 0.29$ . GX 13+1 can be analysed in the same way. The obtained ratio of  $\zeta_1$  is here:  $\zeta_1 = 0.07$  and an upper limit of  $\zeta_1 < 0.35$ . For GX 17+2 we find the lowest crystallinity:  $\zeta_1 = 0.04$  and an upper limit of  $\zeta_1 < 0.17$ . The other sources in the analysis - focussing on 4U 1630-47, GX 340+00 and 4U 1705-44 - show a similar result, although the errors on the dust measurements increase because of the data quality.

As seen above, despite the errors the X-ray binaries with the best signal to noise are best fitted by a mixture of mainly amorphous dust and a contribution of crystalline dust which varies between  $\zeta_1 = 0.04 - 0.12$ . These amounts of crystalline dust are large in comparison with results from the infrared (Section 3.1). An explanation may be found in that we are observing special lines of sight with freshly produced crystalline dust grains that have not fully been amorphized by the processes in the ISM. This result may be in line with the results from the Stardust mission (Westphal et al., 2014), where some of the interstellar silicate dust particles were detected with a crystalline core. However, it is unclear why the X-ray lines of sight towards the central Galactic environment would systematically sample a different environment than the infrared lines of sight.

An alternative explanation for this apparent discrepancy can be found in the different methods used to study the silicate dust. XAFS, especially the features close to the edge, are

sensitive to short range order, whereas, in the infrared, observation are focussed on long range disorder in the dust particles.

There are multiple processes to form crystalline and amorphous dust (e.g., Dorschner et al., 1995; Jäger et al., 2003; Speck et al., 2011). The different techniques used in the laboratory to synthesize amorphous dust show that some of these samples are glassy, others are porous and some samples are not homogeneously amorphous, but show the onsets of crystallisation. All of these samples produce amorphous infrared dust features, albeit with differences in the peak position of the 10 and 18  $\mu\text{m}$  features (Speck et al., 2011). Furthermore, a polycrystalline material can also smear the dust features (Marra et al., 2011) in the infrared and we may thus not perceive sharp crystalline features in the spectrum (Speck et al., 2011). However, the short range crystalline structure between the atoms in a polycrystal are still intact and XAFS may appear in the spectrum. Specifically, even if the material becomes slightly amorphous or glassy, XAFS may still appear in the X-ray spectrum, but are less pronounced and tend to shift with energy when the material becomes more and more disordered (Mastelaro and Zanotto, 2018). Therefore, what may be perceived as amorphous dust in the infrared, can still be observed as crystalline dust in the X-rays. More laboratory research is necessary to make a complete comparison between the crystalline and amorphous dust characteristics in the infrared and the X-rays. On the other hand, high quality astronomical spectra are necessary to put firmer limits on the amount of crystalline dust observed in the spectra of X-ray binaries.

### 3.5.1.2 Iron in silicates

Our sample set contains olivines and pyroxenes with different iron and magnesium content. Already from the laboratory data it can be observed that the influence of a changing iron content of the dust invokes only small differences in the XAFS (Figure 3.1). Small shifts in the peaks can be observed in the laboratory data, but in view of the resolution of the *Chandra* spectra, these subtle changes will not be detected in the spectra. We note that the samples 2, 3, 4, 5 and 6 almost never contribute to the best fit. What these samples have in common is that all of them are iron-poor pyroxenes. Therefore, the reason that these samples do not fit the edge is twofold and the structure of the dust is of greater influence here than the iron content, since the structural differences in the crystal-types can be distinguished in the models. Iron is highly depleted in the ISM and is expected to reside in dust particles. Silicates may provide a possibility to store some of the iron in dust. However, even if our fits prefer slightly more iron-rich silicates, not all the iron that should be present in the ISM is accounted for. The missing iron can be present in other forms of dust. A possibility could be that iron is included in metallic form in GEMS (Bradley, 1994) or in iron nanoparticles (Bilalbegović et al., 2017). Our sample set currently contains pyroxene samples with a ratio of  $\text{Mg}/(\text{Fe}+\text{Mg})=0.6$ . This is very similar to e.g. Kemper et al. (2004) ( $\text{Mg}/(\text{Fe}+\text{Mg})=0.5$ ). Previous studies do not show a strong evidence that this ratio should be much lower. Further constraints on the iron content would be provided by a multiple-edge fitting. The magnesium K-edge and the iron K-edge will give a direct impression of magnesium and iron in dust. Depending on the brightness of the source, the column density along the line of sight and the telescope and instruments that are used, it is possible to observe these edges. In the case of the Fe K-edge, the current instruments are not sensitive enough around the edge to detect the XAFS, but the future observatory, *Athena*, will be able to observe the Fe K-edge in detail (Rogantini et al., 2018).

### 3.5.1.3 Olivines, pyroxenes and oxides

Where the difference between iron rich and iron-poor dust models in the laboratory data is subtle, the difference between olivines, pyroxenes and quartz types in crystalline form is striking. This means that it is easier to identify differences in the mineralogy. In general, we observe that in almost all of the X-ray binaries, the best fitting dust mixture includes an olivine dust type (whether amorphous or crystalline), but not all the data have similar signal to noise. The three X-ray binaries with the best signal-to-noise, namely GX 5-1, GX 17+2 and GX 13+1, show both in the best fit as in the fits within 1 sigma a preference for amorphous olivine. The ratio of olivine to pyroxene can be expressed as  $\zeta_2 = \text{olivine}/(\text{pyroxene} + \text{olivine})$ . For GX 5-1, GX 17+2 and GX 13+1  $\zeta_2 = 1$  in case of the best fits. However, within 1 sigma from the best fitting dust mixtures, it is possible to obtain lower values of  $\zeta_2$  with a minimum of  $\zeta_2 = 0.8$ , meaning that we can obtain a good fit with a maximum of 20% pyroxene in the dust mix.

Thus, in the central Galactic environment we do not find much variation in the best fitting dust mixture. We compare this result with studies of silicates in the infrared. By analyzing the  $10\ \mu\text{m}$  silicate feature, Kemper et al. (2004) also find that olivine glasses account for most of the silicate mass in the diffuse ISM along the line of sight toward the GC. However, in the infrared, variations in the stoichiometry of the dust have been found along different lines of sight. Fitting both the  $10\ \mu\text{m}$  and  $18\ \mu\text{m}$  silicate features of Wolf-Rayet stars representing both the local ISM and the GC, Chiar and Tielens (2006) find that a mix of olivine and pyroxene silicates produce a good match to their data, and that a greater contribution by mass of pyroxene dust is required. Observing the same line of sight as Kemper et al. (2004), Min et al. (2007) find a stoichiometry of the silicate dust that lies in between that of olivine and pyroxene. In future X-ray studies, it is therefore interesting to investigate samples with a stoichiometry in between that of olivine and pyroxene.

The role of  $\text{SiO}_2$  dust in the ISM is not well known. This type of dust may form in the ISM and may be present in the form of  $\text{SiO}_2$  nanoparticles, although there is limited insight of how these dust particles may form and they have not been detected in the ISM (Li and Draine, 2002; Krasnokutski et al., 2014). The presence of  $\text{SiO}_2$  may be supportive of the formation of grains in the interstellar medium (Krasnokutski et al., 2014, and references therein). The three  $\text{SiO}_2$  samples in our sample set, can be fitted within one sigma of the best fit, most notably in 4U 1630-47. Considering the overall contribution of  $\text{SiO}_2$  in the fits of GX 13+1, GX 5-1 and GX 17+2, we do not find evidence for  $\text{SiO}_2$  to be dominant component in interstellar dust.

## 3.5.2 Silicon abundances and depletion

The results from Table 3.3 allow us to study the dense environment in the Galactic plane and in the vicinity of the GC. The abundance of silicon can be derived from infrared data, using observations of the  $10$  and  $18\ \mu\text{m}$  features (Aitken and Roche, 1984; Roche and Aitken, 1985; Tielens et al., 1996). In the local solar environment the silicon abundance in dust can be derived to be  $5.2 \pm 1.8 \times 10^{-5}$  per H-atom, using data from Roche and Aitken (1984); Tielens et al. (1996) who observed nearby Wolf-Rayet stars. On sight lines toward the GC the abundance of silicon in dust is often found to be lower, namely  $3.0 \pm 1.8 \times 10^{-5}$  per H-atom (Roche and Aitken, 1985). This discrepancy may be caused by the presence of large particles ( $> 3\ \mu\text{m}$ )

near the GC. The results of the dust abundance near the GC are also more uncertain, since these infrared silicon abundances depend on an estimate of the visual extinction ( $A_V$ ) derived from  $N_H/A_V$  ratio of the local solar neighborhood (Bohlin et al., 1978) and this method may be more uncertain toward the GC (Tielens et al., 1996). On average our results of the silicate dust abundance,  $4.2 \pm 0.4 \times 10^{-5}$  per H-atom, fall in between the abundances found by Roche and Aitken (1985) to the GC and Roche and Aitken (1984); Tielens et al. (1996) in the local solar environment, but individual lines of sight deviate significantly from the average. We did not find a relation between the silicon dust abundance and the distance of the source from the GC ( $R_{GC}$ ), also called Galactocentric radius. There appears also to be no obvious relations between the abundance of silicon and the distance from the plane of the Galaxy, but this can be attributed to the vicinity of all our sources to the plane.

Besides the abundance of silicon in dust, we can also investigate the total abundance of silicon along the nine lines of sight toward the X-ray binaries. For elements such as Fe, Mg, O and Si, an increase in the abundance toward the GC is observed (Pedicelli et al., 2009; Rolleston et al., 2000; Davies et al., 2009). The vicinity of the X-ray binaries to the GC gives us a unique opportunity to study the behaviour of this gradient in the inner region of the Galaxy, from around 0.9 kpc from the center of the Galaxy. Rolleston et al. (2000) found a Galactic abundance gradient of silicon of  $-0.06 \pm 0.01$  dex/kpc for Galactocentric radii  $R_{GC} > 6$  kpc. For Galactocentric radii  $R_{GC} < 6$  kpc there is no clear gradient was found, as was shown by Davies et al. (2009). They find a gradient for the azimuthal abundance of  $-0.8 \pm 0.1$  dex/kpc for silicon, but the observations have a large scatter. Of course the area of the Galactic bulge provides a different environment from the surrounding Galactic disk. Using Figure 3.5 we can investigate a possible gradient of abundances toward the Galactic plane. Here we show the total abundance of silicon versus  $R_{GC}$ . The abundances obtained from the X-ray binaries are shown in black. The other data points are abundances of silicon of a sample of B-type stars (in purple) from Rolleston et al. (2000) and abundances derived from observations of cepheids (in light blue) from Andrievsky et al. (2002) for comparison. The star symbol at 8.5 kpc indicates the position of the sun and the two yellow bands show the environments of the Galactic bulge and the Galactic molecular ring. The dashed-dotted line shows the solar abundance of silicon. We find a gradient of  $0.06 \pm 0.01$  dex/kpc for the abundances derived from the X-ray binary observations. The gradient is indicated by the dashed line. Instead of the increase of the silicon abundance observed at radii larger than 6 kpc from the center, we observe a slight decrease. We note that the error on this gradient is large and that it can be observed from Figure 3.5 that all the abundances are close to solar. If this decrease is real, it might be caused by an increase of the typical grain size of the silicate grains in the Galactic central area to which the X-rays are not sensitive. In that case the X-rays are a probe for the volume of large grains. This is supported by the observation of a scattering feature just before the edge indicating the possible presence of large grains as described in Chapter 2. However, we also note here, that the error on the distance should also be taken into account before a firm conclusion about the gradient can be made. Furthermore, the errors on the abundance measurements can be reduced by more and longer observations of the sources. In the case of GX 13+1 the errors are already small due to the number of observations we included in the fit and therefore serves as a good example to show the benefit of new observations. All these elements considered, we can conclude that the increase of abundance of silicon at Galactocentric radii  $> 6$  kpc is not observed in the inner part of the Galaxy.

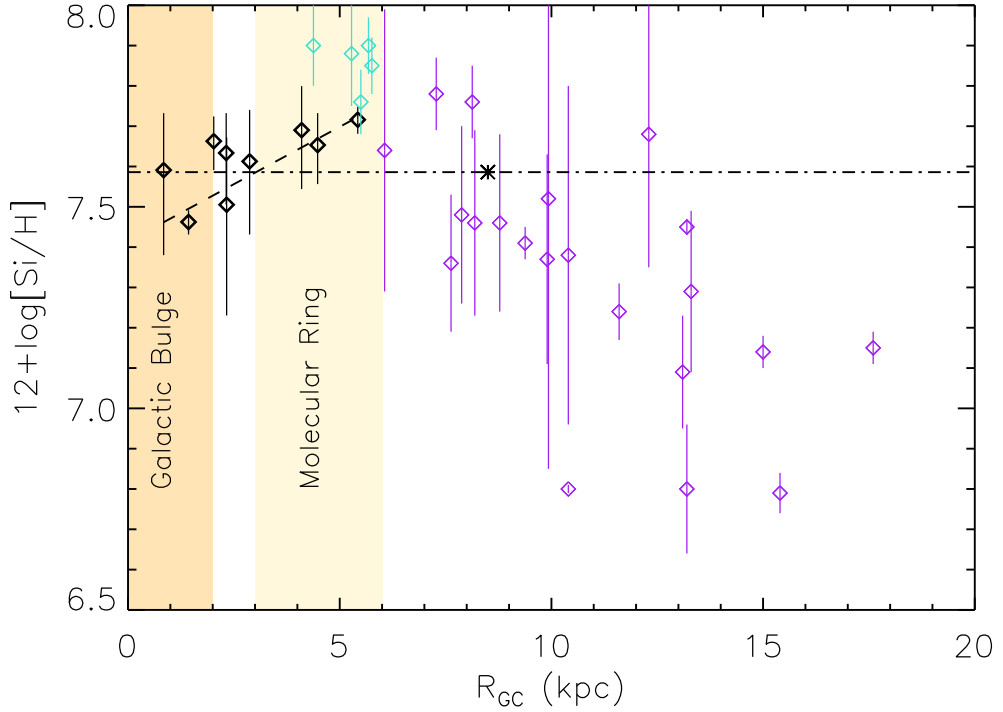


**Figure 3.5:** The total silicon abundance expressed in logarithmic units, with hydrogen by definition 12.0 versus the Galactocentric distance in kpc. The star symbol indicates the position of the Sun and the two yellow bands indicate the position of the Galactic bulge and the molecular ring. The dashed-dotted line indicates the solar abundance and the dashed line the gradient in the abundances obtained from the X-ray nine binaries.

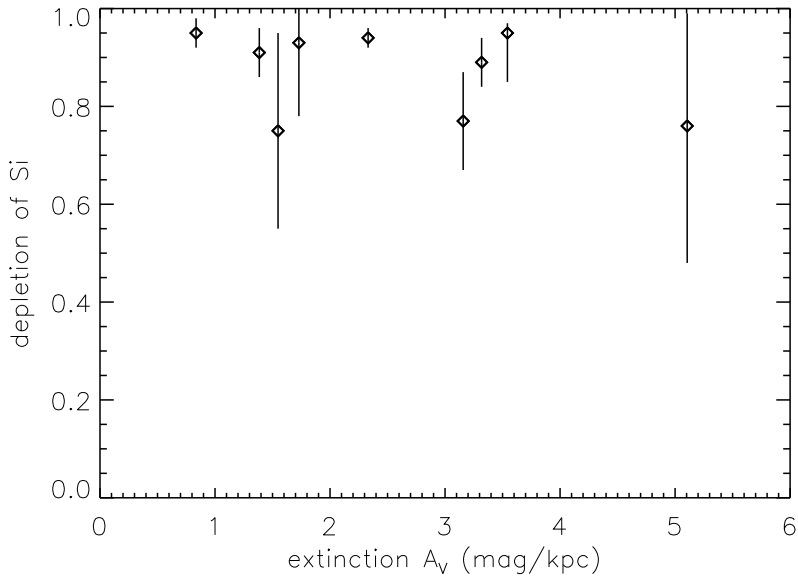


Figure 3.6: Depletion versus visual extinction ( $A_V$ ).

The depletion of elements such as Fe, Mg, O and Si in to dust shows a correlation with the extinction along the line of sight (Jenkins, 2009; Voshchinnikov and Henning, 2010). Where Voshchinnikov and Henning (2010) probe the depletion up to a distance of 7 kpc from the Sun, we are able to observe the depletion of silicon at larger distances and in the less well explored environment of the Galactic central region. Furthermore, we are able to observe both gas and dust simultaneously and in this way we obtain a direct measure of the depletion. Assuming the relation for visual extinction  $N_H/A_V = 1.9 \times 10^{21} \text{cm}^{-2} \text{mag}^{-1}$  (Bohlin et al., 1978), is still valid in the dense environment of the central part of the Galaxy, we obtain the result of the depletions versus the extinction,  $A_V$ , shown in Figure 3.6. Not all of the X-ray binaries follow the average extinction of 2 mag/kpc. Four lines of sight that have extinctions higher than 3 mag/kpc. We do not observe a clear trend in the data. This lack of correlation can be explained by the environment in which the X-ray binaries reside. The central part of the Galaxy has a complex structure as we already noted earlier in this section. All the X-ray binaries are located in this area, so we may be observing local variations in the ISM.

### 3.6 Summary and Conclusion

In this chapter, we fitted the Si edge of of the absorbed spectra along 9 different lines of sight. We used a total of 14 new dust extinction profiles, representing to a good degree the silicate content of the ID. We measured the absorption profiles of these 14 interstellar dust analogues at the Soleil synchrotron facility in Paris. The laboratory absorption measurements were converted into extinction cross-section in order to obtain models for suitable for interstellar dust

studies. We obtained the following results:

- We find that most lines of sight can be well fitted by amorphous olivine. The contribution of crystalline dust to the fits is larger than found in the infrared. For the sources with the best signal-to-noise (i.e. GX 5-1, GX 13+1 and GX 17+2), we find values of the crystallinity range between  $\zeta_1 = 0.04 - 0.12$ , with upper limits on these values of  $\zeta_1$  ranging between 0.17 and 0.35. A possible explanation may lie in the nature of X-rays, which is such that it facilitates to study the short-range order between the atoms, contrary to the long-range disorder in the infrared. In this way, we may observe crystallinity in polycrystalline and partly glassy material. More high quality observations will allow us to put further constraints on this parameter.
- Iron-poor pyroxenes are not preferred in the fits. It is however difficult to put a precise limit on the amount of iron in silicates, since the Si K-edge is not very sensitive to changes in the iron content. In order to investigate the contribution of iron in silicates we need to involve the Fe K-edge. Observations of the Fe K-edge in X-ray binaries will be possible with the future *Athena* observatory. Future studies may therefore benefit from additional iron rich pyroxene dust in the sample set.
- In almost all of the X-ray binaries, the dust mixture best fitting the Si K-edge includes an olivine dust type.
- For the first time, we study the GC environment in the X-rays using the Si K-edge in the spectra of X-ray binaries located in this environment. From the fits, we obtained the total abundance of silicon, the dust abundance and the depletion. We investigated trends for the total abundance versus the Galactocentric distance. Here we observe the local variations in the complex environment of the GC. In the case of the total abundance versus the Galactocentric distance we find a gradient of  $0.06 \pm 0.01$  dex/kpc. We observe a decrease of the silicon abundance toward the GC. This may be caused by silicon atoms locked up in large ( $> 3 \mu\text{m}$ ) dust particles in these dense environments.

## Acknowledgments

Dust studies at Leiden Observatory are supported through the Spinoza Premie of the Dutch science agency, NWO. E.C. and D.R. acknowledge support from NWO-Vidi grant 639.042.525. H.M. and P.M. are grateful for support of the Deutsche Forschungsgemeinschaft under Mu 1164/8-2 and Mu 1164/9-1. We acknowledge SOLEIL for provision of synchrotron radiation facilities and we would like to thank Delphine Vantelon for assistance in using beamline LUCIA. This research made use of the Chandra Transmission Grating Catalog and archive (<http://tgcat.mit.edu>). Furthermore, we made use of the FLUO self absorption correction code provided by Daniel Haskell.

### 3.A Data tables LMXBs

We give a detailed overview of the data obtained from the best fits of X-ray binaries GX 5-1, 4U 1630-47, GX 13+1, 4U 1702-429, 4U 1728-34, GX 340+00, GRS 1758-258, GX 17+2

and 4U 1705-44. In the tables of this section we give the parameters values corresponding to the best fits of each of the sources. The best fits of each of these sources are shown in the corresponding figures.

*GX 5-1*: The fitting of GX 5-1 is explained in Section 3.4.2 for illustration. We found a column density of  $5.8 \pm 0.2 \times 10^{22} \text{cm}^{-2}$ . This value can be compared to previous studies: the column density of GX 5-1 was measured by Predehl and Schmitt (1995) to range between 2.78 and  $3.48 \times 10^{22} \text{cm}^{-2}$  depending on the continuum model. More recent values of the column density are  $2.8 \times 10^{22} \text{cm}^{-2}$  with *Chandra* data by Ueda et al. (2005) and  $3.07 \pm 0.04 \times 10^{22} \text{cm}^{-2}$  by Asai et al. (2000, using ASCA archival data). In Chapter 2 we made use of the short, 0.24 ks, observation of obsid 716 in order to minimize the effect of pile up on the estimate of the column density. This resulted in a column density of  $3.4 \pm 0.1 \times 10^{22} \text{cm}^{-2}$ . These values are lower than the one we find for the spectra used in this study. However, there is a considerable time difference between the observation used in this analysis (July 2017) and the previous observation in TE mode by *Chandra* (July 2000). From the observation listed above, we already note that the observed column density of the source can vary. This variation may be associated to changes over time intrinsic to the source. Such differences in the column density can for instance be observed as well in EXO 0748-676 (van Peet et al., 2009). Furthermore, GX 5-1 deviates from the linear relation between the scattering optical depth and the column density (see Figure 7 of Predehl and Schmitt, 1995). In the case that the interstellar medium is solely responsible for the total amount of absorption, a lower column density is expected for GX 5-1 with respect to the observed scattering optical depth. Since  $N_{\text{H}}$  is observed to be larger, the increase can be associated with the source.

*4U 1630-47*: There are four data sets used in the fitting of the 4U 1630-47 (Table 3.6, Figure 3.7). The source continuum of the source is modelled using two black body models. All observations show outflowing gas, which is modelled by the XABS model. The ionization parameter  $\xi$  in the XABS model is defined as  $\xi = L/nr^2$ , where  $L$  is the ionizing luminosity,  $n$  the gas density and  $r$  the distance of the gas from the source. We find a column density of  $N_{\text{H}} = 9.7 \pm 0.1 \times 10^{22} \text{cm}^{-2}$ , making it the densest line of sight in our study. This value is in agreement with i.a., Neilsen et al. (2014), who find a best-fit column density of  $N_{\text{H}} = 9.4^{+0.5}_{-1.1} \times 10^{22} \text{cm}^{-2}$ .

*GX 13+1*: The continuum of GX 13+1 is fitted with a disk blackbody and Comptonisation model (Table 3.7, Figure 3.8). All the observations have a XABS component, in order to model outflowing gas from the source. In the case of the observation with obsid 11814, a second XABS model is introduced in order to fit the non outflowing ionized gas along the line of sight. The column density of GX 13+1 is in agreement with values found by Pintore et al. (2014) and D’Ai et al. (2014).

*4U 1702-429*: This X-ray binary was modelled using a disk blackbody and a Comptonisation model, resulting in a value of  $N_{\text{H}} 2.3 \pm 0.2 \times 10^{22} \text{cm}^{-2}$ , similar to results found by Iaria et al. (2016) (Table 3.8, Figure 3.9).

*4U 1728-34*: In the case of 4U 1728-34 the continuum was as well modelled by using a disk blackbody and a Comptonisation model (Table 3.8, Figure 3.10). This source is a bursting low mass X-ray binary, and two bursts occur in the spectrum of obsid 2748. These bursts do not affect the modeling of the Si K-edge. The  $N_{\text{H}}$  is in agreement with values found by Di Salvo et al. (2000a) of  $3.1 \pm 0.1 \times 10^{22} \text{cm}^{-2}$ , using a similar modeling and data from the *BeppoSAX* satellite, which covers a wide energy range of 0.12-100 keV, making it especially suitable for

Table 3.5: Best fit parameters for GX 5-1

Obsid	13714	13715
$N_{\text{H}}^{\text{cold}} (10^{22} \text{ cm}^{-2})$	5.8 ± 0.2	
$k_{\text{B}} T_{\text{bb}} (\text{keV})$	0.31 ± 0.01	0.33 ± 0.01
$k_{\text{B}} T_{0 \text{comt}} (\text{keV})$	0.30 ± 0.03	0.30 ± 0.03
$k_{\text{B}} T_{1 \text{comt}} (\text{keV})$	28 ± 9	$23_{-6}^{+12}$
$\tau_{\text{comt}} (\text{keV})$	$1.0_{-0.7}^{+0.2}$	1.2 ± 0.6
$F_{0.5-2 \text{keV}} (10^{-10} \text{ erg cm}^{-2} \text{ s}^{-1})$	3.8 ± 0.4	3.6 ± 0.4
$F_{2-10 \text{keV}} (10^{-8} \text{ erg cm}^{-2} \text{ s}^{-1})$	1.8 ± 0.2	1.7 ± 0.2
$C^2/\nu$	2026/1603	

This fit was produced using the following SPEX models: a blackbody model, a Comptonisation model, the AMOL model, cold gas model (HOT with  $k_{\text{B}} T = 5 \times 10^{-4}$ ) and XABS.

hydrogen column density measurements.

*GX 340+00*: is well fitted by a powerlaw model in combination with a blackbody model. We added a Gaussian model in order to fit the iron  $K_{\alpha}$  emission-line feature around 6.4 keV. The obtained column density of hydrogen is:  $6.6 \pm 0.2 \times 10^{22} \text{ cm}^{-2}$ . This value is similar to results from Seifina et al. (2013), who make use of data from *BeppoSAX* and *RXTE* and find values of  $\sim 5.5 - 6.5 \times 10^{22} \text{ cm}^{-2}$  for several models. It is below values found by (Cackett et al., 2010) of  $0.9 - 1.1 \times 10^{23} \text{ cm}^{-2}$  using *XMM-Newton* data.

*GRS 1758-258*: The continuum of GRS 1758-258 is best fitted by a blackbody and a steep power law function (Smith et al., 2001) (Table 3.9, Figure 3.12).

*GX 17+2*: The continuum of GX 17+2 modelled using a blackbody model in combination with powerlaw function (Table 3.9, Figure 3.13). The column density is estimated by Cackett et al. (2009) to lie between  $3.12 \pm 0.05$  and  $4.63 \pm 0.08 \times 10^{22} \text{ cm}^{-2}$ , using *Chandra* data. This column density is higher than the value found in our analysis of  $2.0 \pm 0.1 \times 10^{22} \text{ cm}^{-2}$ . However, our analysis is in agreement with the analysis of Di Salvo et al. (2000b), who use data from *BeppoSAX*.

*4U 1705-44*: The continuum of 4U 1705-44 is also modelled using a blackbody model in combination with powerlaw function (Table 3.9, Figure 3.14). The column density is in agreement with data from *BeppoSAX* (Piraino et al., 2016, model 2).

### 3.B Si K-edge models

Figure 3.15 shows the extinction profiles around the Si K-edge for the compounds 1 to 14, see Table 3.1. All the profiles are implemented in the AMOL model of the spectral fitting code SPEX. The absolute cross-sections of the models used in this analysis are available in tabular form on the following website: [www.sron.nl/~elisa/VIDI/](http://www.sron.nl/~elisa/VIDI/). Furthermore, we show the laboratory edges from Figure 3.1 in individual panels for comparison in Figure 3.16.

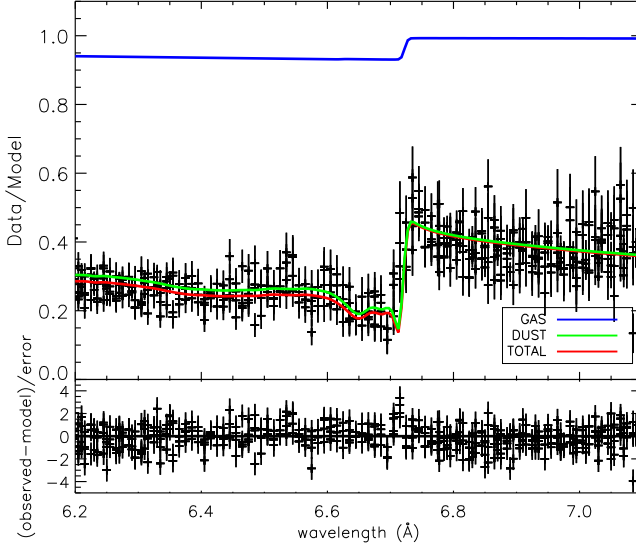


Figure 3.7: Si K-edge of 4U 1630-47.

Table 3.6: Best fit parameters for 4U 1630-47

Obsid	13714	13715	13716	13717
$N_{\text{H}}^{\text{cold}} (10^{22} \text{ cm}^{-2})$			$9.7 \pm 0.1$	
$k_{\text{B}} T_{\text{bb1}} (\text{keV})$	$0.62 \pm 0.01$	$0.62 \pm 0.01$	$0.60 \pm 0.01$	$0.63 \pm 0.01$
$k_{\text{B}} T_{\text{bb2}} (\text{keV})$	$1.2 \pm 0.3$	$1.2 \pm 0.4$	$1.2 \pm 0.4$	$1.2 \pm 0.5$
$N_{\text{H}}^{\text{xabs}} (10^{22} \text{ cm}^{-2})$			$9.2 \pm 0.2$	
$\log \xi^{\text{xabs}} (\text{erg cm s}^{-1})$			$4.1 \pm 0.2$	
$z v_{\text{out}}^{\text{xabs}} (10^2 \text{ kms}^{-1})$			$-1.0^{+1.3}_{-1.0}$	
$N_{\text{H}}^{\text{xabs2}} (10^{22} \text{ cm}^{-2})$			$9.0 \pm 0.2$	
$\log \xi^{\text{xabs2}} (\text{erg cm s}^{-1})$			$4.3 \pm 0.1$	
$z v_{\text{out}}^{\text{xabs2}} (10^2 \text{ kms}^{-1})$			$-7.8 \pm 0.3$	
$F_{0.5-2 \text{ keV}} (10^{-12} \text{ erg cm}^{-2} \text{ s}^{-1})$	$8.2 \pm 2$	$8.2 \pm 2.0$	$7.8 \pm 1.9$	$8.0 \pm 1.8$
$F_{2-10 \text{ keV}} (10^{-9} \text{ erg cm}^{-2} \text{ s}^{-1})$	$4.1 \pm 0.9$	$4.0 \pm 0.9$	$3.8 \pm 0.8$	$4.4 \pm 0.9$
$C^2/\nu$			$5258/4028$	

This fit was produced using the following SPEX models: two blackbody models, the AMOL model, cold gas model (HOT with  $k_{\text{B}} T = 5 \times 10^{-4}$ ) and two XABS models. Both XABS models are coupled to the four observations, since these observations were performed in succession.

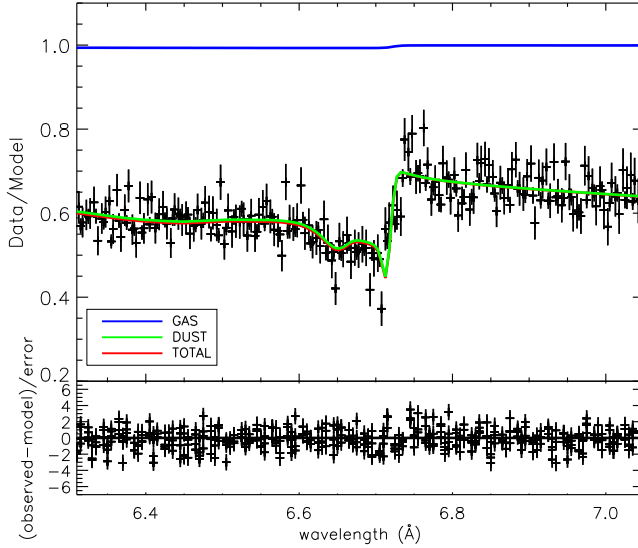


Figure 3.8: Si K-edge GX 13+1.

Table 3.7: Best fit parameters for GX 13+1

Obsid	11814	11815	11816	11817
$N_{\text{H}}^{\text{cold}} (10^{22} \text{ cm}^{-2})$		$3.1 \pm 0.1$		
$k_{\text{B}} T_{\text{dbb}} (\text{keV})$	$0.72 \pm 0.18$	$0.99 \pm 0.06$	$0.87 \pm 0.25$	$0.32 \pm 0.14$
$k_{\text{B}} T_{0 \text{comt}} (\text{keV})$	$0.70 \pm 0.03$	$0.79 \pm 0.03$	$0.80 \pm 0.06$	$0.70 \pm 0.02$
$k_{\text{B}} T_{1 \text{comt}} (\text{keV})$	$12 \pm 3$	$11 \pm 2$	$12_{-3}^{+8}$	$11 \pm 1$
$\tau_{\text{comt}} (\text{keV})$	$1.4 \pm 0.2$	$0.54 \pm 0.09$	$0.20_{-0.19}^{+0.30}$	$1.9_{-0.6}^{+0.4}$
$N_{\text{H}}^{\text{xabs1}} (10^{23} \text{ cm}^{-2})$	$1.1 \pm 0.1$	$1.8 \pm 0.1$	$4.1 \pm 0.1$	$3.2 \pm 0.1$
$\log \xi^{\text{xabs1}}$	$4.3 \pm 0.5$	$4.3 \pm 0.3$	$4.3 \pm 0.1$	$4.5 \pm 0.1$
$z v_{\text{out}}^{\text{xabs1}} (10^2 \text{ kms}^{-1})$	$-4.4_{-5.3}^{+3.0}$	$-5.5_{-1.5}^{+1.9}$	$-6.2_{-2.1}^{+3.7}$	$-3.5 \pm 1.4$
$N_{\text{H}}^{\text{xabs2}} (10^{21} \text{ cm}^{-2})$	$1.1 \pm 0.2$	-	-	-
$\log \xi^{\text{xabs2}} (\text{erg cm s}^{-1})$	$3.0 \pm 0.1$	-	-	-
$z v^{\text{xabs2}} (10^2 \text{ kms}^{-1})$	$> -0.1$	-	-	-
$F_{0.5-2 \text{ keV}} (10^{-10} \text{ erg cm}^{-2} \text{ s}^{-1})$	$1.4 \pm 0.1$	$1.8 \pm 0.2$	$1.8 \pm 0.2$	$1.6 \pm 0.2$
$F_{2-10 \text{ keV}} (10^{-9} \text{ erg cm}^{-2} \text{ s}^{-1})$	$5.6 \pm 0.6$	$6.6 \pm 0.7$	$6.5 \pm 0.7$	$6.8 \pm 0.7$
$C^2/\nu$	5910/4738			

This fit was produced using the following SPEX model components: a disk blackbody, a Comptonisation model, the AMOL model, cold gas model (i.e. HOT with  $k_{\text{B}} T = 5 \times 10^{-4}$ ) and two XABS models.

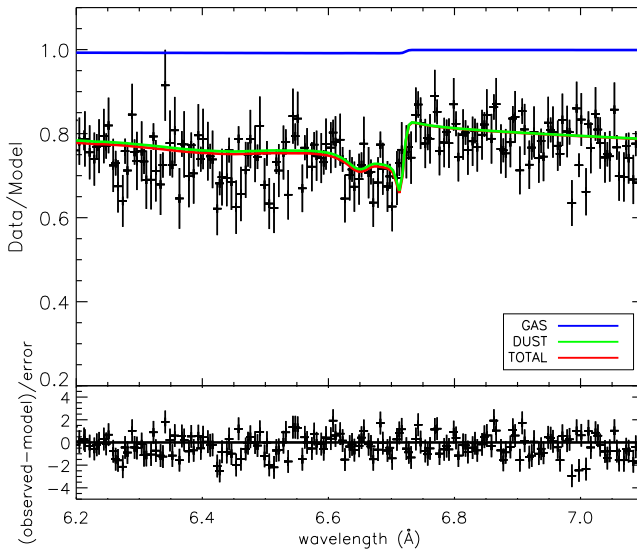


Figure 3.9: Si K-edge 4U 1702-429.

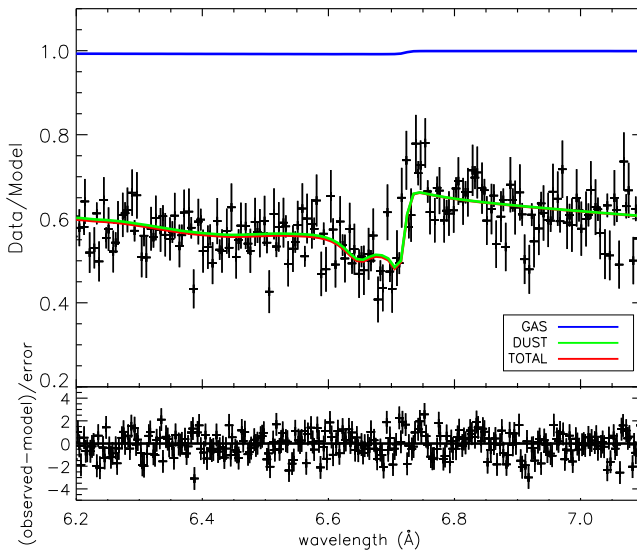


Figure 3.10: Si K-edge 4U 1728-34.

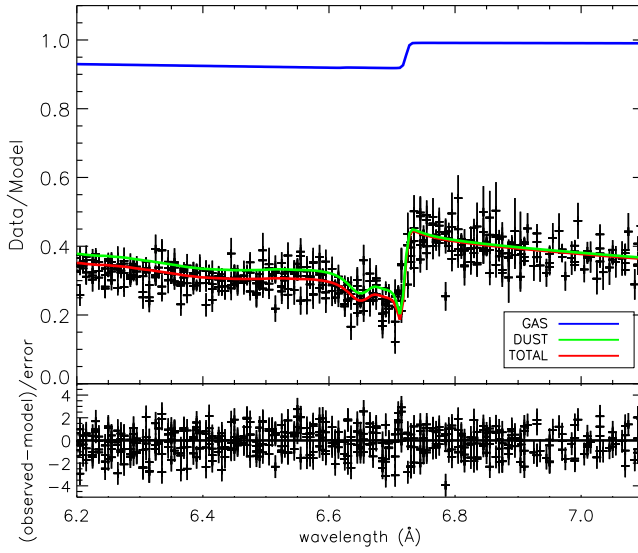


Figure 3.11: Si K-edge GX 340+00.

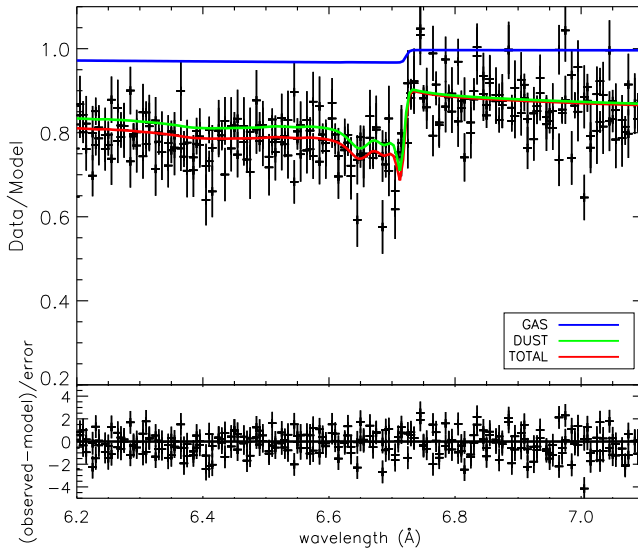


Figure 3.12: Si K-edge GRS 1758-258.

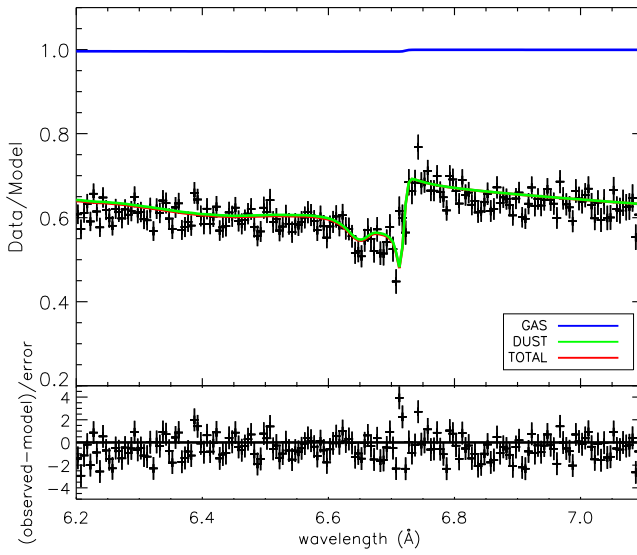


Figure 3.13: Si K-edge GX 17+2.

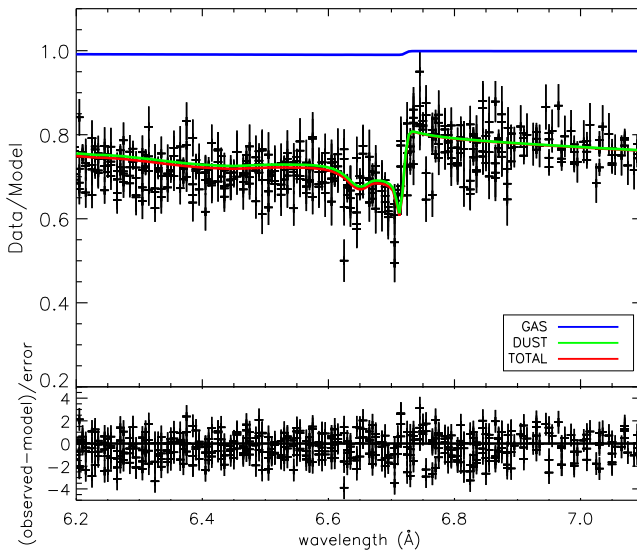


Figure 3.14: Si K-edge 4U 1705-44.

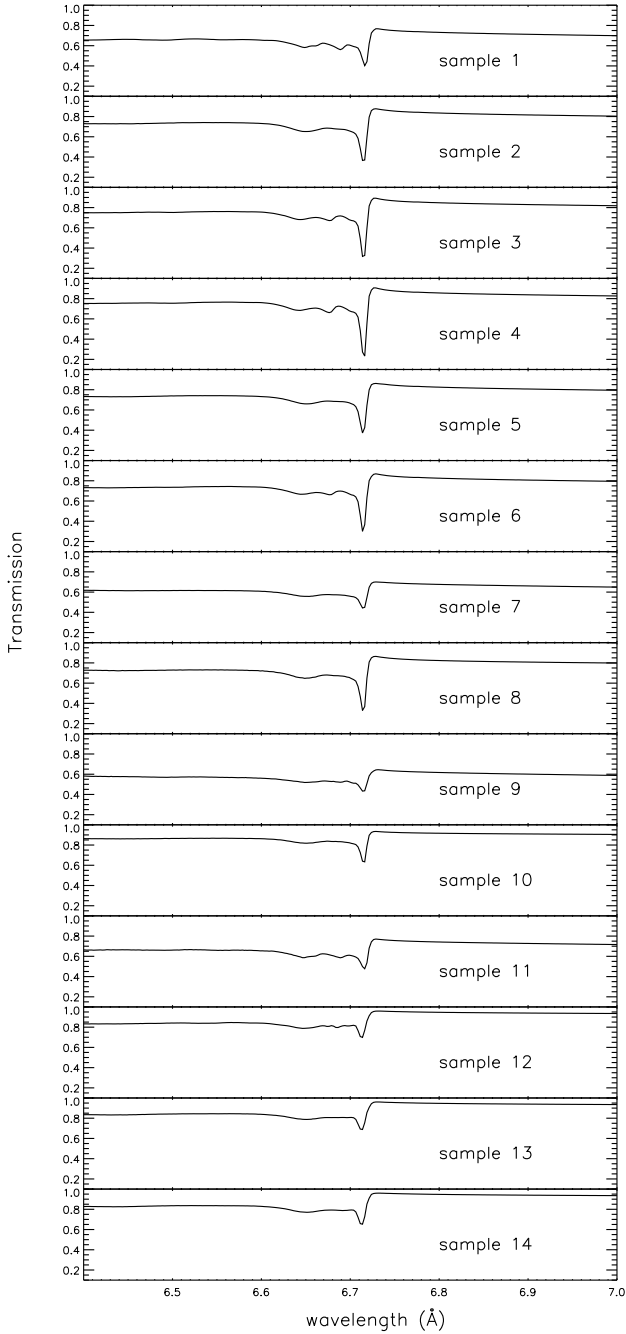


Figure 3.15: Transmission of the six dust extinction models (absorption and scattering) of the Si K-edge. The silicon column density has been set here to  $10^{18} \text{ cm}^{-2}$  for all the dust models. Each model is indicated by a number which corresponds to the numbers in Table 3.1.

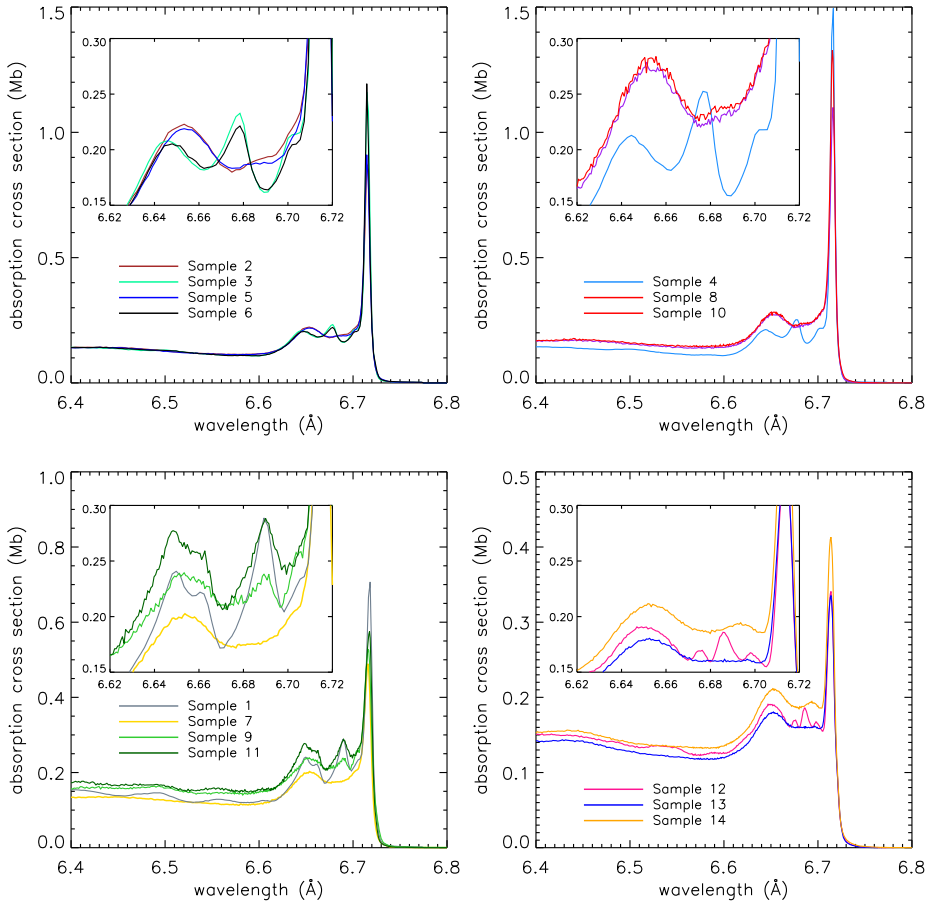


Figure 3.16: The Si K-edge of dust samples 1-14, see Table 3.1. The x-axis shows the energy in Å and the y-axis shows the amount of absorption indicated by the cross-section (in Mb per Si atom). The samples are shown in different panels for easier comparison. The top left panel shows the difference between amorphous and crystalline pyroxenes (i.e. samples 2, 3, 5 and 6). The top right panel shows the difference between amorphous and crystalline enstatite (samples 4 and 10), including as well an amorphous pyroxene. The bottom left panel focusses on the olivine dust samples and the bottom right panel shows our three quartz samples.

Table 3.8: Best fit parameters for 4U 1702-429, 4U 1728-34 and GX 340+00

Source	4U 1702-429	4U 1728-34	GX 340+00			
Obsid	11045	2748	1921	18085	19450	20099
$N_{\text{cold}}$ ( $10^{22} \text{ cm}^{-2}$ )	$2.3 \pm 0.2$	$3.5^{+0.2}_{-0.5}$		$6.6 \pm 0.2$		
$k_B T_{\text{hb}}$ (keV)	-	-	$2.1^{+0.7}_{-0.1}$	$1.1 \pm 0.1$	$1.0 \pm 0.1$	$1.0 \pm 0.1$
$\Gamma_{\text{pow}}$	-	-	$1.6 \pm 0.1$	$1.5 \pm 0.1$	$2.0 \pm 0.1$	$1.8 \pm 0.1$
$k_B T_{\text{dhh}}$ (keV)	$0.74^{+0.22}_{-0.10}$	$0.27^{+0.01}_{-0.05}$	-	-	-	-
$E_{\text{gauss}}$ (keV)	-	-	$6.6 \pm 0.1$	-	$6.4 \pm 0.1$	$6.3 \pm 0.1$
$FWHM_{\text{gauss}}$ (keV)	-	-	$0.40 \pm 0.08$	-	$2.3^{+0.2}_{-0.1}$	$2.9 \pm 0.2$
$k_B T_{0 \text{ compt}}$	$0.47^{+0.21}_{-0.07}$	$0.44^{+0.05}_{-0.10}$	-	-	-	-
$k_B T_{1 \text{ compt}}$ (keV)	$2.5^{+0.3}_{-0.2}$	$2.1^{+0.5}_{-0.17}$	-	-	-	-
$\tau_{\text{compt}}$	$7.0^{+9.3}_{-0.6}$	$2.5^{+3.4}_{-2.1}$	-	-	-	-
$F_{0.5-2 \text{ keV}}$ ( $10^{-11} \text{ erg cm}^{-2} \text{ s}^{-1}$ )	$5.6 \pm 1.0$	$0.8 \pm 0.1$	$2.5 \pm 0.2$	$4.0 \pm 0.4$	$4.3 \pm 0.3$	$4.4 \pm 0.3$
$F_{2-10 \text{ keV}}$ ( $10^{-9} \text{ erg cm}^{-2} \text{ s}^{-1}$ )	$0.6 \pm 0.1$	$1.7 \pm 0.1$	$6.2 \pm 0.4$	$10 \pm 1$	$7.6 \pm 0.5$	$9.4 \pm 0.7$
$\chi^2/\nu$	2350/2144	1403/1326		4777/3954		

The fit of 4U 1702-429 was produced using the following SPEX model components: a disk blackbody, a Comptonisation model, AMOL model, cold gas model (i.e. HOT with  $k_B T = 5 \times 10^{-4}$ ) and XABS model.

The fit of 4U 1728-34 was produced using the following SPEX model components: a disk blackbody, a Comptonisation model, AMOL, cold gas model and XABS. The fit of GX 340+00 was produced using the following SPEX models: a blackbody, power-law, AMOL, cold gas model and XABS.

Table 3.9: Best fit parameters for GRS 1758-258, GX 17+2 and 4U 1705-44

Source	GRS 1758-258		GX 17+2		4U 1705-44		
Obsid	2429	2750	11088	5500	18086	19451	20082
$N_{\text{H}}^{\text{cold}}$ ( $10^{22} \text{ cm}^{-2}$ )		$2.5 \pm 0.1$				$2.0 \pm 0.1$	
$N_{\text{H}}^{\text{hot}}$ ( $10^{20} \text{ cm}^{-2}$ )		$2.4^{+3.4}$				$0.29^{+0.18}$	
$k_{\text{B}} T_{\text{hot}}$ (keV)		$1.3^{+0.5}$				$0.28^{+0.23}$	
$k_{\text{B}} T_{\text{bb}}$ (keV)	$0.38 \pm 0.01$	$0.42 \pm 0.01$	-	-	-	$0.28^{+0.18}$	-
$\Gamma_{\text{pow}}$	$3.9^{+0.1}$	$2.7 \pm 0.1$	-	-	-	-	-
$T_{\text{dbb}}$ (keV)	-	-	$1.7^{+0.2}$	$0.42^{+0.07}$	$0.99^{+0.16}$	$0.53^{+0.18}$	$0.43^{+0.08}$
$k_{\text{B}} T_{0,\text{comt}}$ (keV)	-	-	$0.60 \pm 0.01$	$0.41 \pm 0.01$	$0.65^{+0.03}$	$0.54 \pm 0.02$	$0.49 \pm 0.01$
$k_{\text{B}} T_{1,\text{comt}}$ (keV)	-	-	$30^{+6}$	$21^{+20}$	$47^{+39}$	$40^{+53}$	$18^{+22}$
$\tau_{\text{comt}}$	-	-	$1.7^{+1.1}$	$1.4^{+1.6}$	$0.9^{+1.8}$	$1.0^{+1.6}$	$1.6^{+1.2}$
$F_{0.5-2 \text{ keV}}$ ( $10^{-10} \text{ erg cm}^{-2} \text{ s}^{-1}$ )	$0.8 \pm 0.2$	$1.2 \pm 0.2$	$4.3 \pm 0.8$	$1.4 \pm 0.1$	$3.6 \pm 0.4$	$2.3 \pm 0.2$	$2.3 \pm 0.2$
$F_{2-10 \text{ keV}}$ ( $10^{-9} \text{ erg cm}^{-2} \text{ s}^{-1}$ )	$0.12 \pm 0.04$	$0.44 \pm 0.08$	$13 \pm 2$	$1.7 \pm 0.2$	$7.1 \pm 0.7$	$3.9 \pm 0.4$	$3.0 \pm 0.3$
$C^2/\nu$	4182/3770		1393/1109		5838/4459		

The fit of GRS 1758-258 was produced using the following SPEX model components: a blackbody, power-law, AMOL, cold gas model (i.e. HOT with  $k_{\text{B}} T = 5 \times 10^{-4}$ ) and hot gas (HOT).

The fit of GX 17+2 was produced using the following SPEX model components: a disk blackbody, a comptonisation, AMOL, cold gas model and hot gas (HOT).

The fit of 4U 1705-44 was produced using the following SPEX model components: a disk blackbody, a comptonisation, AMOL, cold gas model and hot gas (HOT).



## References

- Aitken, D. K. and Roche, P. F. (1984). A study of the unidentified dust emission features near 10 microns. *MNRAS*, 208:751–761.
- Andrievsky, S. M., Bersier, D., Kovtyukh, V. V., Luck, R. E., Maciel, W. J., Lépine, J. R. D., and Beletsky, Y. V. (2002). Using Cepheids to determine the galactic abundance gradient. II. Towards the galactic center. *A&A*, 384:140–144.
- Asai, K., Dotani, T., Nagase, F., and Mitsuda, K. (2000). Iron K Emission Lines in the Energy Spectra of Low-Mass X-Ray Binaries Observed with ASCA. *ApJS*, 131:571–591.
- Augusteijn, T., Kuulkers, E., and van Kerkwijk, M. H. (2001). The IR counterpart of the black-hole candidate 4U 1630-47. *A&A*, 375:447–454.
- Bandyopadhyay, R. M., Shahbaz, T., Charles, P. A., and Naylor, T. (1999). Infrared spectroscopy of low-mass X-ray binaries - II. *MNRAS*, 306:417–426.
- Bilalbegović, G., Maksimović, A., and Mohaček-Grošev, V. (2017). Missing Fe: hydrogenated iron nanoparticles. *MNRAS*, 466:L14–L18.
- Bohlin, R. C., Savage, B. D., and Drake, J. F. (1978). A survey of interstellar H I from L-alpha absorption measurements. II. *ApJ*, 224:132–142.
- Bohren, C. F. (2010). What did kramers and kronig do and how did they do it? *European Journal of Physics*, 31(3):573.
- Bradley, J. P. (1994). Chemically Anomalous, Preaccretionally Irradiated Grains in Interplanetary Dust From Comets. *Science*, 265:925–929.
- Bringa, E. M., Kucheyev, S. O., Loeffler, M. J., Baragiola, R. A., Tielens, A. G. G. M., Dai, Z. R., Graham, G., Bajt, S., Bradley, J. P., Dukes, C. A., Felter, T. E., Torres, D. F., and van Breugel, W. (2007). Energetic Processing of Interstellar Silicate Grains by Cosmic Rays. *ApJ*, 662:372–378.
- Bruzzoni, P., Carranza, R., Lacoste, J. C., and Crespo, E. (2002). Kramers?kronig transforms calculation with a fast convolution algorithm. *Electrochimica Acta*, 48(4):341 – 347.
- Cackett, E. M., Miller, J. M., Ballantyne, D. R., Barret, D., Bhattacharyya, S., Boutelier, M., Miller, M. C., Strohmayer, T. E., and Wijnands, R. (2010). Relativistic Lines and Reflection from the Inner Accretion Disks Around Neutron Stars. *ApJ*, 720:205–225.

- Cackett, E. M., Miller, J. M., Homan, J., van der Klis, M., Lewin, W. H. G., Méndez, M., Raymond, J., Steeghs, D., and Wijnands, R. (2009). A Search for Iron Emission Lines in the Chandra X-Ray Spectra of Neutron Star Low-Mass X-Ray Binaries. *ApJ*, 690:1847–1855.
- Cash, W. (1979). Parameter estimation in astronomy through application of the likelihood ratio. *ApJ*, 228:939–947.
- Chen, L., Hou, J. L., and Wang, J. J. (2003). On the Galactic Disk Metallicity Distribution from Open Clusters. I. New Catalogs and Abundance Gradient. *AJ*, 125:1397–1406.
- Chiar, J. E. and Tielens, A. G. G. M. (2006). Pixie Dust: The Silicate Features in the Diffuse Interstellar Medium. *ApJ*, 637:774–785.
- Christian, D. J. and Swank, J. H. (1997). The Survey of Low-Mass X-Ray Binaries with the Einstein Observatory Solid-State Spectrometer and Monitor Proportional Counter. *ApJS*, 109:177–224.
- Costantini, E. and de Vries, C. P. (2013). Characterizing the chemistry of interstellar dust: the X-ray view. *Mem. Soc. Astron. Italiana*, 84:592.
- Costantini, E., Pinto, C., Kaastra, J. S., in't Zand, J. J. M., Freyberg, M. J., Kuiper, L., Méndez, M., de Vries, C. P., and Waters, L. B. F. M. (2012). XMM-Newton observation of 4U 1820-30. Broad band spectrum and the contribution of the cold interstellar medium. *A&A*, 539:A32.
- D'Ai, A., Iaria, R., Di Salvo, T., Riggio, A., Burderi, L., and Robba, N. R. (2014). Chandra X-ray spectroscopy of a clear dip in GX 13+1. *A&A*, 564:A62.
- Davies, B., Origlia, L., Kudritzki, R.-P., Figer, D. F., Rich, R. M., Najarro, F., Negueruela, I., and Clark, J. S. (2009). Chemical Abundance Patterns in the Inner Galaxy: The Scutum Red Supergiant Clusters. *ApJ*, 696:2014–2025.
- de Groot, F. M. F. (2012). Dips and peaks in fluorescence yield X-ray absorption are due to state-dependent decay. *Nature*, 4:766–767.
- de Vries, C. P. and Costantini, E. (2009). Physical properties of amorphous solid interstellar material from X-ray absorption spectroscopy of <ASTROBJ>Scorpius X-1</ASTROBJ>. *A&A*, 497:393–398.
- Di Salvo, T., Iaria, R., Burderi, L., and Robba, N. R. (2000a). The Broadband Spectrum of MXB 1728-34 Observed by BeppoSAX. *ApJ*, 542:1034–1040.
- Di Salvo, T., Stella, L., Robba, N. R., van der Klis, M., Burderi, L., Israel, G. L., Homan, J., Campana, S., Frontera, F., and Parmar, A. N. (2000b). The Discovery of a State-Dependent Hard Tail in the X-Ray Spectrum of the Luminous Z Source GX 17+2. *ApJ*, 544:L119–L122.

- Dorschner, J., Begemann, B., Henning, T., Jaeger, C., and Mutschke, H. (1995). Steps toward interstellar silicate mineralogy. II. Study of Mg-Fe-silicate glasses of variable composition. *A&A*, 300:503.
- Draine, B. T. (2003). Scattering by Interstellar Dust Grains. II. X-Rays. *ApJ*, 598:1026–1037.
- Draine, B. T. and Lee, H. M. (1984). Optical properties of interstellar graphite and silicate grains. *ApJ*, 285:89–108.
- Fabian, D., Henning, T., Jäger, C., Mutschke, H., Dorschner, J., and Wehrhan, O. (2001). Steps toward interstellar silicate mineralogy. VI. Dependence of crystalline olivine IR spectra on iron content and particle shape. *A&A*, 378:228–238.
- Flank, A.-M., Cauchon, G., Lagarde, P., Bac, S., Janousch, M., Wetter, R., Dubuisson, J.-M., Idir, M., Langlois, F., Moreno, T., and D. Vantelon, D. (2006). LUCIA, a microfocus soft XAS beamline. *Nuclear Instruments and Methods in Physics Research Section B: Beam Interactions with Materials and Atoms*, 246(1):269–274. Synchrotron Radiation and Materials Science.
- Galloway, D. K., Munro, M. P., Hartman, J. M., Psaltis, D., and Chakrabarty, D. (2008). Thermonuclear (Type I) X-Ray Bursts Observed by the Rossi X-Ray Timing Explorer. *ApJS*, 179:360–422.
- Henning, T. (2010). Cosmic Silicates. *ARA&A*, 48:21–46.
- Henning, T., Begemann, B., Mutschke, H., and Dorschner, J. (1995). Optical properties of oxide dust grains. *A&AS*, 112:143.
- Iaria, R., Di Salvo, T., Del Santo, M., Pintore, F., Sanna, A., Papitto, A., Burderi, L., Riggio, A., Gambino, A. F., and Matranga, M. (2016). Study of the reflection spectrum of the LMXB 4U 1702–429. *A&A*, 596:A21.
- Jäger, C., Fabian, D., Schrempel, F., Dorschner, J., Henning, T., and Wesch, W. (2003). Structural processing of enstatite by ion bombardment. *A&A*, 401:57–65.
- Jenkins, E. B. (2009). A Unified Representation of Gas-Phase Element Depletions in the Interstellar Medium. *ApJ*, 700:1299–1348.
- Kaastra, J. S. (2017). On the use of C-stat in testing models for X-ray spectra. *A&A*, 605:A51.
- Kaastra, J. S., de Vries, C. P., Costantini, E., and den Herder, J. W. A. (2009). Effective area calibration of the reflection grating spectrometers of XMM-Newton. I. X-ray spectroscopy of the Crab nebula. *A&A*, 497:291–310.
- Kaastra, J. S., Mewe, R., and Nieuwenhuijzen, H. (1996). SPEX: a new code for spectral analysis of X & UV spectra. In Yamashita, K. and Watanabe, T., editors, *UV and X-ray Spectroscopy of Astrophysical and Laboratory Plasmas*, pages 411–414.

- Keck, J. W., Craig, W. W., Hailey, C. J., Harrison, F., Hong, J. S., Kahn, S. M., Lubin, P. M., McLean, R., Pivovarov, M. J., Seiffert, M., Wurtz, R., and Zioc, K. P. (2001). Long-Term Multiwavelength Observations of GRS 1758-258 and the Advection-dominated Accretion Flow Model. *ApJ*, 563:301–312.
- Kemper, F., Vriend, W. J., and Tielens, A. G. G. M. (2004). The Absence of Crystalline Silicates in the Diffuse Interstellar Medium. *ApJ*, 609:826–837.
- Krasnokutski, S. A., Rouillé, G., Jäger, C., Huisken, F., Zhukovska, S., and Henning, T. (2014). Formation of Silicon Oxide Grains at Low Temperature. *ApJ*, 782:15.
- Lee, J. C., Ogle, P. M., Canizares, C. R., Marshall, H. L., Schulz, N. S., Morales, R., Fabian, A. C., and Iwasawa, K. (2001). Revealing the Dusty Warm Absorber in MCG -6-30-15 with the Chandra High-Energy Transmission Grating. *ApJ*, 554:L13–L17.
- Lee, J. C., Xiang, J., Ravel, B., Kortricht, J., and Flanagan, K. (2009). Condensed Matter Astrophysics: A Prescription for Determining the Species-specific Composition and Quantity of Interstellar Dust Using X-rays. *ApJ*, 702:970–979.
- Li, A. and Draine, B. T. (2002). Are Silicon Nanoparticles an Interstellar Dust Component? *ApJ*, 564:803–812.
- Lin, D., Remillard, R. A., Homan, J., and Barret, D. (2012). The Spectral Evolution along the Z Track of the Bright Neutron Star X-Ray Binary GX 17+2. *ApJ*, 756:34.
- Lingenberg, D. (1986). PhD thesis, University of Frankfurt/M.
- Lodders, K. and Palme, H. (2009). Solar System Elemental Abundances in 2009. *Meteoritics and Planetary Science Supplement*, 72:5154.
- Marra, A. C., Lane, M. D., Orofino, V., Blanco, A., and Fonti, S. (2011). Midinfrared spectra and optical constants of bulk hematite: Comparison with particulate hematite spectra. *Icarus*, 211:839–848.
- Mastelaro, V. and Zanotto, E. (2018). X-ray Absorption Fine Structure (XAFS) Studies of Oxide Glasses - A 45-Year Overview. *Materials*, 11:204.
- Mie, G. (1908). Beiträge zur Optik trüber Medien, speziell kolloidaler Metallösungen. *Annalen der Physik*, 330:377–445.
- Min, M., Waters, L. B. F. M., de Koter, A., Hovenier, J. W., Keller, L. P., and Markwick-Kemper, F. (2007). The shape and composition of interstellar silicate grains. *A&A*, 462:667–676.
- Molster, F. J., Waters, L. B. F. M., Tielens, A. G. G. M., and Barlow, M. J. (2002). Crystalline silicate dust around evolved stars. I. The sample stars. *A&A*, 382:184–221.
- Neilsen, J., Coriat, M., Fender, R., Lee, J. C., Ponti, G., Tzioumis, A. K., Edwards, P. G., and Broderick, J. W. (2014). A Link between X-Ray Emission Lines and Radio Jets in 4U 1630-47? *ApJ*, 784:L5.

- Nittler, L. R. (2005). Constraints on Heterogeneous Galactic Chemical Evolution from Meteoritic Stardust. *ApJ*, 618:281–296.
- Oosterbroek, T., Penninx, W., van der Klis, M., van Paradijs, J., and Lewin, W. H. G. (1991). EXOSAT observations of the X-ray burst source 4U 1702 - 42. *A&A*, 250:389–394.
- Parmar, A. N., Stella, L., and White, N. E. (1986). The evolution of the 1984 outburst of the transient X-ray source 4U 1630 - 47. *ApJ*, 304:664–670.
- Pedicelli, S., Bono, G., Lemasle, B., François, P., Groenewegen, M., Lub, J., Pel, J. W., Laney, D., Piersimoni, A., Romaniello, M., Buonanno, R., Caputo, F., Cassisi, S., Castelli, F., Leurini, S., Pietrinferni, A., Primas, F., and Pritchard, J. (2009). On the metallicity gradient of the Galactic disk. *A&A*, 504:81–86.
- Pinto, C., Kaastra, J. S., Costantini, E., and de Vries, C. (2013). Interstellar medium composition through X-ray spectroscopy of low-mass X-ray binaries. *A&A*, 551:A25.
- Pinto, C., Kaastra, J. S., Costantini, E., and Verbunt, F. (2010). High-resolution X-ray spectroscopy of the interstellar medium. XMM-Newton observation of the LMXB GS 1826-238. *A&A*, 521:A79.
- Pintore, F., Sanna, A., Di Salvo, T., Guainazzi, M., D’Ai, A., Riggio, A., Burderi, L., Iaria, R., and Robba, N. R. (2014). Testing rate-dependent corrections on timing mode EPIC-pn spectra of the accreting neutron star GX 13+1. *MNRAS*, 445:3745–3754.
- Piraino, S., Santangelo, A., Mück, B., Kaaret, P., Di Salvo, T., D’Ai, A., Iaria, R., and Egron, E. (2016). Broadband observations of the X-ray burster 4U1705-44 with BeppoSAX. *A&A*, 591:A41.
- Posch, T., Kerschbaum, F., Mutschke, H., Dorschner, J., and Jäger, C. (2002). On the origin of the 19.5  $\mu$  m feature. Identifying circumstellar Mg-Fe-oxides. *A&A*, 393:L7–L10.
- Predehl, P. and Schmitt, J. H. M. M. (1995). X-raying the interstellar medium: ROSAT observations of dust scattering halos. *A&A*, 293:889–905.
- Ravel, B. and Newville, M. (2005). *ATHENA, artemis, hephaestus*: data analysis for x-ray absorption spectroscopy using *ifeffit*. *Journal of Synchrotron Radiation*, 12(4):537–541.
- Roche, P. F. and Aitken, D. K. (1984). An investigation of the interstellar extinction. I - Towards dusty WC Wolf-Rayet stars. *MNRAS*, 208:481–492.
- Roche, P. F. and Aitken, D. K. (1985). An investigation of the interstellar extinction. II - Towards the mid-infrared sources in the Galactic centre. *MNRAS*, 215:425–435.
- Rogantini, D., Costantini, E., Zeegers, S. T., de Vries, C. P., Bras, W., de Groot, F., Mutschke, H., and Waters, L. B. F. M. (2018). Investigating the interstellar dust through the Fe K-edge. *A&A*, 609:A22.
- Rolleston, W. R. J., Smartt, S. J., Dufton, P. L., and Ryans, R. S. I. (2000). The Galactic metallicity gradient. *A&A*, 363:537–554.

- Savage, B. D. and Sembach, K. R. (1996). Interstellar Abundances from Absorption-Line Observations with the Hubble Space Telescope. *ARA&A*, 34:279–330.
- Seifina, E., Titarchuk, L., and Frontera, F. (2013). Stability of the Photon Indices in Z-source GX 340+0 for Spectral States. *ApJ*, 766:63.
- Smith, D. M., Heindl, W. A., Swank, J. H., and Markwardt, C. B. (2001). Black-Hole Candidate GRS 1758-258 Enters an “Off” State. *The Astronomer’s Telegram*, 66.
- Speck, A. K., Pitman, K. M., and Hofmeister, A. M. (2015). Better Alternatives to “Astronomical Silicate”: Laboratory-based Optical Functions of Chondritic/Solar Abundance Glass with Application to HD 161796. *ApJ*, 809:65.
- Speck, A. K., Whittington, A. G., and Hofmeister, A. M. (2011). Disordered Silicates in Space: A Study of Laboratory Spectra of “Amorphous” Silicates. *ApJ*, 740:93.
- Stern, E., Newville, M., Ravel, B., Yacoby, Y., and Haskel, D. (1995). The {UWXAFS} analysis package: philosophy and details. *Physica B: Condensed Matter*, 208-209:117–120. Proceedings of the 8th International Conference on X-ray Absorption Fine Structure.
- Sylvester, R. J., Kemper, F., Barlow, M. J., de Jong, T., Waters, L. B. F. M., Tielens, A. G. G. M., and Omont, A. (1999). 2.4-197  $\mu$ m spectroscopy of OH/IR stars: the IR characteristics of circumstellar dust in O-rich environments. *A&A*, 352:587–599.
- Tielens, A. G. G. M. (2001). The Composition of Circumstellar and Interstellar Dust. In Woodward, C. E., Bica, M. D., and Shull, J. M., editors, *Tetons 4: Galactic Structure, Stars and the Interstellar Medium*, volume 231 of *Astronomical Society of the Pacific Conference Series*, page 92.
- Tielens, A. G. G. M., Wooden, D. H., Allamandola, L. J., Bregman, J., and Witteborn, F. C. (1996). The Infrared Spectrum of the Galactic Center and the Composition of Interstellar Dust. *ApJ*, 461:210.
- Ueda, Y., Mitsuda, K., Murakami, H., and Matsushita, K. (2005). Study of the Galactic Interstellar Medium from High-Resolution X-Ray Spectroscopy: X-Ray Absorption Fine Structure and Abundances of O, Mg, Si, S, and Fe. *ApJ*, 620:274–286.
- Valencic, L. A. and Smith, R. K. (2013). Interstellar Abundances toward X Per, Revisited. *ApJ*, 770:22.
- van Peet, J. C. A., Costantini, E., Méndez, M., Paerels, F. B. S., and Cottam, J. (2009). Properties of the ionised plasma in the vicinity of the neutron-star X-ray binary EXO 0748-676. *A&A*, 497:805–813.
- Voshchinnikov, N. V. and Henning, T. (2010). From interstellar abundances to grain composition: the major dust constituents Mg, Si, and Fe. *A&A*, 517:A45.
- Wang, Q. D. (2009). Global Hot Gas in and around the Galaxy. In Smith, R. K., Snowden, S. L., and Kuntz, K. D., editors, *American Institute of Physics Conference Series*, volume 1156 of *American Institute of Physics Conference Series*, pages 257–267.

- Wang, Q. D., Nowak, M. A., Markoff, S. B., Baganoff, F. K., Nayakshin, S., Yuan, F., Cuadra, J., Davis, J., Dexter, J., Fabian, A. C., Grosso, N., Haggard, D., Houck, J., Ji, L., Li, Z., Neilsen, J., Porquet, D., Ripple, F., and Shcherbakov, R. V. (2013). Dissecting X-ray-Emitting Gas Around the Center of Our Galaxy. *Science*, 341:981–983.
- Weingartner, J. C. and Draine, B. T. (2001). Dust Grain-Size Distributions and Extinction in the Milky Way, Large Magellanic Cloud, and Small Magellanic Cloud. *ApJ*, 548:296–309.
- Westphal, A. J., Stroud, R. M., Bechtel, H. A., Brenker, F. E., Butterworth, A. L., Flynn, G. J., Frank, D. R., Gainsforth, Z., Hillier, J. K., Postberg, F., Simionovici, A. S., Sterken, V. J., Nittler, L. R., Allen, C., Anderson, D., Ansari, A., Bajt, S., Bastien, R. K., Bassim, N., Bridges, J., Brownlee, D. E., Burchell, M., Burghammer, M., Changela, H., Cloetens, P., Davis, A. M., Doll, R., Floss, C., Grün, E., Heck, P. R., Hoppe, P., Hudson, B., Huth, J., Kearsley, A., King, A. J., Lai, B., Leitner, J., Lemelle, L., Leonard, A., Leroux, H., Lettieri, R., Marchant, W., Oglione, R., Ong, W. J., Price, M. C., Sandford, S. A., Tresseras, J.-A. S., Schmitz, S., Schoonjans, T., Schreiber, K., Silversmit, G., Solé, V. A., Srama, R., Stadermann, F., Stephan, T., Stodolna, J., Sutton, S., Trieloff, M., Tsou, P., Tyliczszak, T., Vekemans, B., Vincze, L., Von Korff, J., Wordsworth, N., Zevin, D., Zolensky, M. E., and aff14 (2014). Evidence for interstellar origin of seven dust particles collected by the Stardust spacecraft. *Science*, 345:786–791.
- Wiscombe, W. J. (1980). Improved mie scattering algorithms. *Appl. Opt.*, 19(9):1505–1509.
- Yao, Y., Schulz, N., Wang, Q. D., and Nowak, M. (2006). Chandra Detection of Fe XVII in Absorption: Iron Abundance in the Hot Gaseous Interstellar Medium. *ApJ*, 653:L121–L124.
- Yao, Y. and Wang, Q. D. (2005). X-Ray Absorption Line Spectroscopy of the Galactic Hot Interstellar Medium. *ApJ*, 624:751–764.
- Yao, Y. and Wang, Q. D. (2007). The Galactic Central Diffuse X-Ray Enhancement: A Differential Absorption/Emission Analysis. *ApJ*, 666:242–246.
- Zeegers, S. T., Costantini, E., de Vries, C. P., Tielens, A. G. G. M., Chihara, H., de Groot, F., Mutschke, H., Waters, L. B. F. M., and Zeidler, S. (2017). Absorption and scattering by interstellar dust in the silicon K-edge of GX 5-1. *A&A*, 599:A117.
- Zeidler, S., Posch, T., and Mutschke, H. (2013). Optical constants of refractory oxides at high temperatures. Mid-infrared properties of corundum, spinel, and  $\alpha$ -quartz, potential carriers of the 13  $\mu\text{m}$  feature. *A&A*, 553:A81.

